Mechanical Implications of Creep and Partial Coupling on the World's Fastest Slipping Low-angle Normal Fault in Southeastern Papua New Guinea

James B. Biemiller[1], Carolyn Boulton[2], Laura Wallace[3], Susan Ellis[4], Timothy Little[2], Marcel Mizera[5], André Niemeijer[5], and Luc L Lavier[6]

[1]University of Texas at Austin
[2]Victoria University of Wellington
[3]GNS Science
[4]Geological and Nuclear Sciences
[5]Utrecht University
[6]Department of Geological Sciences, Institute for Geophysics, University of Texas at Austin

November 24, 2022

Abstract

We use densely spaced campaign GPS observations and laboratory friction experiments on fault rocks from one of the world's most rapidly slipping low-angle normal faults, the Mai'iu fault in Papua New Guinea, to investigate the nature of interseismic deformation on active low-angle normal faults. GPS velocities reveal 8.3±1.2 mm/yr of horizontal extension across the Mai'iu fault, and are fit well by dislocation models with shallow fault locking (above 2 km depth), or by deeper locking (from ~5-16 km depth) together with shallower creep. Laboratory friction experiments show that gouges from the shallowest portion of the fault zone are predominantly weak and velocity-strengthening, while fault rocks deformed at greater depths are stronger and velocity-weakening. Evaluating the geodetic and friction results together with geophysical and microstructural evidence for mixed-mode seismic and aseismic slip at depth, we find that the Mai'iu fault is most likely strongly locked at depths of ~5-16 km and creeping updip and downdip of this region. Our results suggest that the Mai'iu fault and other active low-angle normal faults can slip in large (M > 7) earthquakes despite near-surface interseismic creep on frictionally stable clay-rich gouges.

Mechanical Implications of Creep and Partial Coupling on the World's Fastest Slipping Low-angle Normal Fault in Southeastern Papua New Guinea

James Biemiller[1], Carolyn Boulton[2], Laura Wallace[1,3], Susan Ellis[3], Timothy Little[2], Marcel Mizera[2,4], Andre Niemeijer[4], Luc Lavier[1]

[1] Institute for Geophysics, Jackson School of Geosciences, University of Texas at Austin, Austin, Texas, USA.

[2] School of Geography, Environment and Earth Sciences, Victoria University of Wellington, Wellington, New Zealand.

[3] GNS Science, Lower Hutt, New Zealand.

[4] Faculty of Geosciences, Utrecht University, Utrecht, The Netherlands.

Corresponding author: James Biemiller (james.biemiller@utexas.edu)

Key Points:

- GPS velocities reveal horizontal extension of 8.3±1.2 mm/yr (~8-11 mm/yr dip-slip) on a low-angle normal fault dipping ≤24° at the surface
- Shallowest gouges of this fault are frictionally weak and velocity-strengthening; deeper fault rocks are stronger and velocity-weakening
- Fault locking at ~5-16 km depth with shallower and deeper interseismic creep inferred from geologic, experimental, and geodetic results

Abstract (<250 words)

We use densely spaced campaign GPS observations and laboratory friction experiments on fault rocks from one of the world's most rapidly slipping low-angle normal faults, the Mai'iu fault in Papua New Guinea, to investigate the nature of interseismic deformation on active low-angle normal faults. GPS velocities reveal 8.3±1.2 mm/yr of horizontal extension across the Mai'iu fault, and are fit well by dislocation models with shallow fault locking (above 2 km depth), or by deeper locking (from ~5-16 km depth) together with shallower creep. Laboratory friction experiments show that gouges from the shallowest portion of the fault zone are predominantly weak and velocity-strengthening, while fault rocks deformed at greater depths are stronger and velocity-weakening. Evaluating the geodetic and friction results together with geophysical and microstructural evidence for mixed-mode seismic and aseismic slip at depth, we find that the Mai'iu fault is most likely strongly locked at depths of ~5-16 km and creeping updip and downdip of this region. Our results suggest that the Mai'iu fault and other active low-angle normal faults can slip in large (M_w > 7) earthquakes despite near-surface interseismic creep on frictionally stable clay-rich gouges.

Plain Language Summary

In regions of extension, where tectonic plates pull apart, the Earth's crust breaks along fractures, or 'normal faults,' that allow parts of the crust to slip past each other. Many of these faults intersect the Earth's surface at a steep angle, but some anomalously low-angle normal faults are oriented at a shallower angle to the surface. Faults can slip during infrequent fast earthquakes or through slower gradual fault creep. Because active low-angle normal faults are rare and typically have low long-term slip-rates, it is not clear whether they cause large earthquakes or creep gradually. Using two approaches, this study addresses whether earthquakes occur on one of the fastest-slipping of these types of faults, the Mai'iu fault in Papua New Guinea. One approach uses GPS measurements to track patterns of displacement of the Earth's surface near the Mai'iu fault over three years. Surface displacements confirm that the Mai'iu fault slips actively and are used to constrain models of fault slip at depth. The second approach uses laboratory experiments on rocks from the Mai'iu fault zone to test whether these rocks tend to slip unstably in earthquakes, or creep stably under conditions similar to those in the fault zone. Laboratory results show that rocks from the shallowest parts of the fault tend to creep stably, while deeper fault rocks tend to slip unstably. Combining

laboratory, geological and GPS results to map slip behaviors to different fault zone depths, we find that the Mai'iu fault most likely creeps near the Earth's surface but can generate larger earthquakes at greater depths.

1.1. Introduction

Active continental rift systems accommodate extension at rates ranging from <1 mm/yr to a few cm/yr (Abers, 2001; Ruppel, 1995). This extension is facilitated by a variety of seismic and aseismic deformation processes on normal faults, including slip in devastating M_w 6+ earthquakes such as the 6 April 2009 L'Aquila event in Italy that killed over 300 people (Anzidei et al., 2009). Some extending regions, such as the Gulf of Corinth and the Apennines, experience frequent earthquakes on steeply dipping (>40°) near-surface fault sections (Abers, 2009; Jackson, 1987; Jackson & McKenzie, 1983). In these same systems, there is also evidence for aseismic creep on other, less steeply-dipping normal faults (Abers, 2009; Hreinsdóttir & Bennett, 2009; Valoroso et al., 2017). Extensional systems commonly consist of a series of near-surface high-angle (dipping 40-70°) normal faults that are at least in part seismogenic, and that sole into a deeper low-angle (<30°) to sub-horizontal detachment fault, which may creep aseismically (Abers, 2009; Collettini, 2011; Wernicke, 1995).

The mechanics of initiation and subsequent slip of detachment faults dipping at low angles (<30°) near the Earth's surface are not fully understood. These 'low-angle normal faults' (LANFs) appear to defy Mohr-Coulomb friction theory. This theory posits that under a vertical maximum principal stress, normal faults formed in the brittle crust with Byerlee values of friction should initiate at dips of 60-70° and should frictionally lock up and stop slipping at dips <30° (e.g., Axen, 1992, 2004; Wernicke, 1995). However, geologic offsets of ~10 km or more on shallowly dipping detachments are commonly observed globally (e.g., Wernicke, 1995; Collettini, 2011; Platt et al., 2015), and a variety of seismological, geodetic and geologic observations indicate that some LANFs are active today (e.g., Abers, 2001, 2009; Anderlini et al., 2016; Chiaraluce et al., 2007, 2014; Collettini, 2011; Hreinsdóttir & Bennett, 2009; Numelin et al., 2007a; Valoroso et al., 2017; Wallace et al., 2014; Webber et al., 2018). Dip slip rates of active and inactive LANFs range from <1 to 10s of mm/yr (Webber et al., 2018). The mechanical paradox of slip on LANFs is most apparent at or near the Earth's surface, where the maximum principal stress is likely to be near-vertical and deformation is assumed to occur predominantly by brittle, frictional failure (e.g., Abers, 2009).

A longstanding and societally important question is whether LANFs can generate large earthquakes and, if so, how frequently (e.g., Wernicke, 1995). The instrumental record of M_w > 5.5 normal-fault earthquakes with unambiguously discriminated rupture planes is sparse (Collettini et al., 2019; Jackson & White, 1989), but it includes two events in the Gulf of Corinth with reported dips as low as 30° and 33°, and with magnitudes of 5.9 and 6.2, respectively. Other earthquakes with indiscriminate nodal planes are inferred to reflect LANF slip based on their seismological and geological context (Collettini, 2011), including the notable 29 October 1985 M_w 6.8 Woodlark Basin earthquake. This event occurred around a seismologically imaged LANF, aligned parallel to one of the focal planes, and may be the largest LANF earthquake documented globally (Abers, 2001; Abers et al., 1997).

Due to the rarity and typically low slip rates (a few mm/yr or less) of active LANFs (Webber et al., 2018), geodetic observations across them are scarce and can be difficult to interpret. However, available results indicate some degree of aseismic creep on the active Altotiberina LANF in the Northern Appenines, Italy (Anderlini et al., 2016; Chiaraluce et al., 2014; Hreinsdóttir & Bennett, 2009; Valoroso et al., 2017). GPS velocities have been used to infer that this fault actively slips at 1.5 mm/yr (Anderlini et al., 2016) to 2.4 mm/yr (Hreinsdóttir & Bennett, 2009). Slip on the Altotiberina fault occurs either by partial creep on a fault that is heterogeneously coupled in space (Anderlini et al., 2016), or by aseismic creep below a locking depth of 4 km (Hreinsdóttir & Bennett, 2009).

A variety of mechanisms have been proposed for aseismic creep on LANFs. These include: 1) an enhanced tendency for stable slip resulting from elevated pore-fluid pressures (Axen, 1992; Collettini & Barchi, 2004; Ikari et al., 2009; Abers, 2009); 2) rotated principal stress orientations favoring slip on low-angle faults (Axen, 1992, 2019); and/or 3) creep on interconnected networks of frictionally stable minerals (e.g., Collettini, 2011; Collettini et al., 2019) such as talc (Collettini et al., 2009a), clays (Ikari et al., 2009; Ikari & Kopf, 2017) or serpentine (antigorite/lizardite) (Floyd et al., 2001). It remains unclear whether fault rocks composed of these frictionally stable mineralogies are abundant on active LANFs; and, in particular, whether they are present (or thermodynamically stable) at the depths where LANFs are inferred to be creeping. One promising approach to understanding mechanisms of LANF slip involves the integration of friction experiments and microstructural analyses of rocks exhumed along an active LANF with corresponding geodetic observations of surface deformation around the same fault. Such an integrated approach has the potential to illuminate the mechanics and spatial extent of active LANF slip. Evaluating these disparate datasets in tandem can help connect geodetic signals of LANF slip to geologically and experimentally constrained deformation mechanisms.

Here, we address the question of whether LANFs creep aseismically or slip in earthquakes following periods of locking and interseismic elastic strain accumulation by presenting and modeling data from a dense campaign GPS network spanning the world's most rapidly slipping active LANF, the Mai'iu fault in southeast Papua New Guinea (PNG; Webber et al., 2018). To strengthen our interpretation of the geodetic data, we perform hydrothermal velocity-stepping friction experiments on exhumed samples from different parts of the Mai'iu fault rock sequence under a range of relevant crustal conditions. Our results complement new microstructural observations of deformation mechanisms within the Mai'iu fault rocks in Mizera et al. (submitted). Geological and geodetic evidence suggests that the Mai'iu fault slips at dip-slip rates of ~10 mm/yr (Wallace et al., 2014; Webber et al., 2018). The Mai'iu fault is therefore an ideal natural laboratory in which to use both geology and geodesy to study the nature of interseismic deformation on an active crustal-scale, misoriented fault. We employ detailed geodetic surveys, elastic dislocation modelling techniques, and laboratory friction experiments on rocks from the Mai'iu fault to address the mechanics and seismic behavior of a rapidly slipping, active LANF.

1.2. Tectonic and geological setting of the Mai'iu fault

The Woodlark Rift in southeast PNG is a young, actively propagating rift located within a region of microplates between the converging Pacific and Australian plates (Figure 1a; Baldwin et al., 2012 and references within) and is well-known for hosting active low-angle normal faults near its westward transition from oceanic spreading to continental rifting (Abers, 1991, 2001; Abers et al., 1997, 2016; Little et al., 2007). Northward subduction of Solomon Sea oceanic lithosphere at the San Cristobal and New Britain trenches drives rapid counterclockwise rotation of the Woodlark and Trobriand microplates at 2–2.7°/Myr relative to Australia about nearby Euler poles to the SW (Figure 1a), yielding primarily N-S extension in the Woodlark Rift. Extension rates range from 20–35 mm/yr in the eastern Woodlark spreading center to 5–15 mm/yr in the onshore continental portion of the rift in the Papuan Peninsula and D'Entrecasteaux Islands

(Wallace et al., 2014). Recent seismicity is focused just west of the oceanic-continental rift transition, following the Woodlark Rise westward through the D'Entrecasteaux Islands (Abers et al., 1997, 2016). This seismicity commonly aligns with geologically mapped and/or geodetically inferred active normal faults or strike-slip transfer faults (Little et al., 2007, 2011; Wallace et al., 2014). From Goodenough Island west to Cape Vogel, microseismicity focused in the upper 15 km along a WSW-trending corridor termed the Ward Hunt Strait fault zone delineates a possible actively deforming transfer zone in continental crust near the Papuan Peninsula (Abers et al., 2016; Figure 1b). Few shallow (<12 km) earthquakes have been observed to the west of the Ward Hunt Strait fault zone, where most extension appears to collapse onto a single fault—the low-angle Mai'iu fault. Offshore to the northeast of the Mai'iu fault trace, aligned microseismicity from 12-25 km depth outlines a 30-40°-dipping planar zone inferred to be the downdip extent of the Mai'iu fault (Abers et al., 2016).

Dipping ~21° where it intersects the Earth's surface, the Mai'iu fault is the dominant mapped fault in the continental Woodlark rift between 149.0–149.6°E (Figure 1; Abers et al., 2016; Mizera et al., 2019; Little et al., 2019; Wallace et al., 2014). The footwall of the Mai'iu fault hosts the actively exhuming Dayman-Suckling metamorphic core complex, a smoothly corrugated domal structure exposing very low-grade (pumpellyite-actinolite-facies) rocks near its ~3 km-high crest and higher-temperature (greenschist-facies) rocks along its northern margin near sea level (Daczko et al., 2009; Little et al., 2019). The Mai'iu fault juxtaposes metabasaltic rocks—the Goropu Metabasalt—in its footwall against ultramafic rocks of the Papuan Ultramafic Belt, and structurally above, unmetamorphosed conglomeratic rocks in its hanging wall (e.g., Little et al., 2019; Mizera et al., submitted). Over the past few Myr, the Mai'iu fault is inferred to have slipped at ~12 mm/yr, based on the slip-parallel width (at least 30 km) of exhumed fault remnants atop the Dayman-Suckling metamorphic core complex and the exposure at >2 km elevation of 2–3 Ma syn-extensional granites in the footwall that were originally buried at depths of 4–10 km (Little et al., 2019; Mizera et al., 2019; Österle et al., 2020). In addition, accumulation of cosmogenic nuclides in quartz veins on the exhumed fault scarp of the Mai'iu fault indicate Holocene to present-day dip-slip rates of 11.7±3.5 mm/yr (Webber et al., 2018). For a 21° dip, modern dip-slip rates of 7.5–9.6 mm/yr across the Mai'iu fault have been estimated from a regional-scale network of GPS velocities (Wallace et al., 2014) and agree well with geologic slip rates.

Minor synthetic and antithetic splay faults in the hanging wall of the Mai'iu fault are presumed to intersect the active fault at depths of up to a few km (Figure 1; Little et al., 2019; Mizera et al., 2019). The most prominent of these, the Gwoira fault, cuts the upper ~1 km of the Mai'iu fault hanging wall east of Mt. Dayman (Webber et al., 2020). Inception of this splay fault led to abandonment of the shallowest portion of the Mai'iu fault farther south. East of the Gwoira fault, the Mai'iu fault system steps offshore and remains active along the southern Goodenough Bay coastline, as evidenced by Holocene uplift of coral reef terraces at rates of up to 4.3 mm/yr (Biemiller et al., 2018; Mann & Taylor, 2002; Mann et al., 2009). The well-preserved platform-notch-platform morphology and clustered $^{230}Th/^{234}U$ ages of these emerged reefs reflect episodic and presumably coseismic meter-scale uplift events, suggesting that the Goodenough Bay segment of the Mai'iu fault system slips in moderately large ($M_w > 7$) earthquakes (Biemiller et al., 2018).

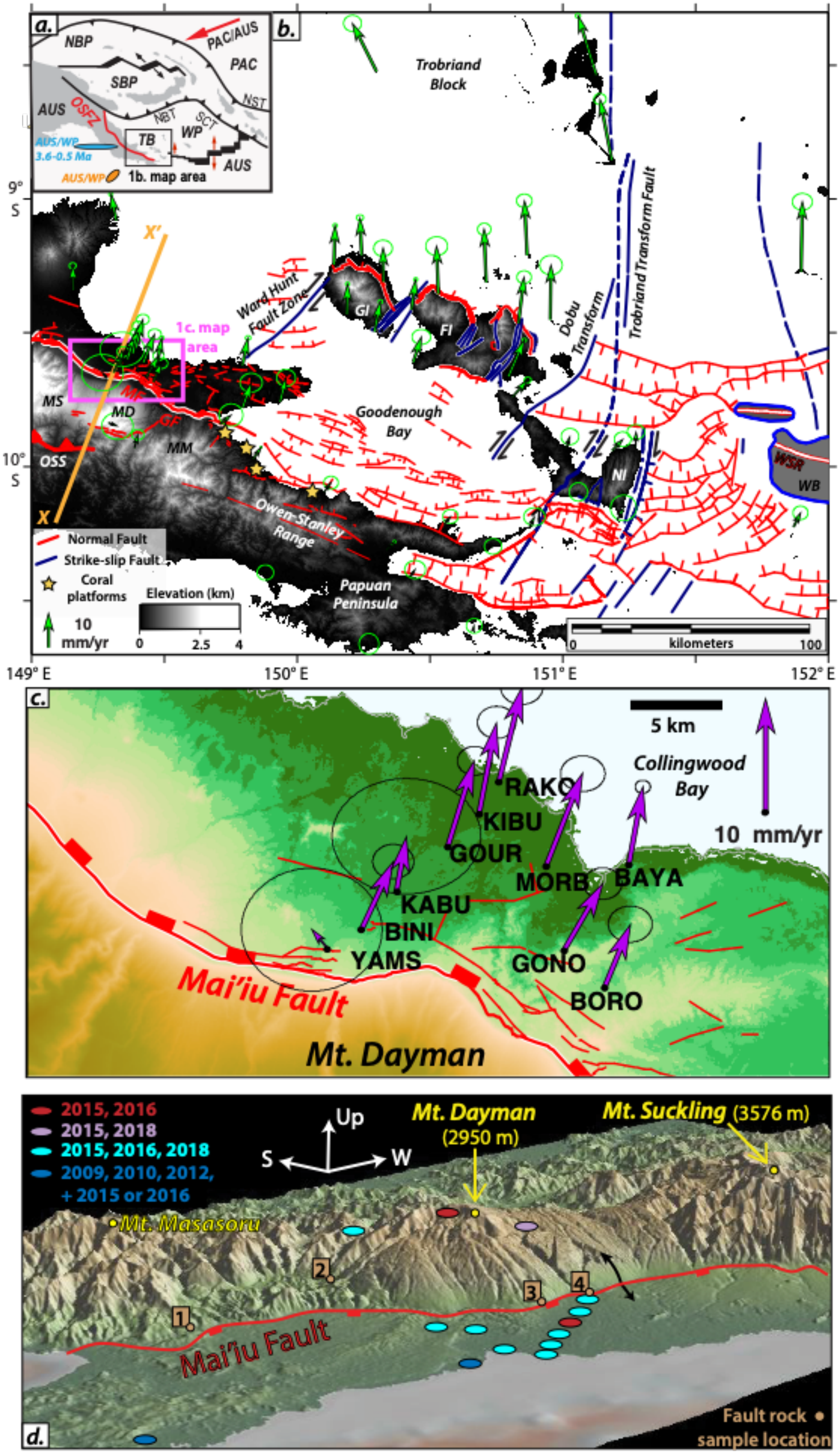
a.
NBP
PAC/AUS
PAC
SBP
NST
AUS
OSFZ
NBT
SCT
WP
TB
AUS/WP 3.6-0.5 Ma
AUS/WP
1b. map area
AUS
b.
Trobriand Block
Ward Hunt Fault Zone
GI
FI
Dobu Transform
Trobriand Transform Fault
1c. map area
MS
MD
MF
GF
OSS
MM
Goodenough Bay
NI
WSR
WB
Owen-Stanley Range
Papuan Peninsula
Normal Fault
Strike-slip Fault
Coral platforms
10 mm/yr
Elevation (km)
0
2.5
4
0
kilometers
100
9° S
10° S
149° E
150° E
151° E
152° E
c.
5 km
Collingwood Bay
10 mm/yr
RAKO
KIBU
GOUR
MORB
BAYA
KABU
BINI
YAMS
GONO
BORO
Mai'iu Fault
Mt. Dayman
2015, 2016
2015, 2018
2015, 2016, 2018
2009, 2010, 2012, + 2015 or 2016
Up
S
W
Mt. Dayman (2950 m)
Mt. Suckling (3576 m)
Mt. Masasoru
1
2
3
4
Mai'iu Fault
Fault rock sample location
d.

Figure 1. a.) Regional tectonic map of PNG with main map area outlined, showing overall Australia-Pacific Plate convergence and Woodlark spreading (vectors). Ellipses show modern (orange; Wallace et al., 2014) and 3.6–0.5 Ma (cyan; Taylor et al., 1999) poles of rotation of the Woodlark Plate relative to the Australian Plate. b.) Topographic map with faults from Little et al. (2007, 2011, 2019) and GPS velocities relative to the Australian Plate (section 2; Wallace et al., 2014). Ellipses show 95% confidence intervals based on formal uncertainties. Stars indicate uplifted Holocene coral platforms. Dashed box shows area of 1c. c.) Enlarged map of dense GPS velocity field on the Mai'iu fault hanging wall. d.) Oblique view of the Mai'iu fault and Dayman-Suckling Metamorphic Core Complex (Mt. Masasoru, Mt. Dayman, and Mt. Suckling). Black arrows show sense of motion across the fault. Ellipse colors show observation years at GPS sites near the fault (see key), and brown circles show fault rock sample locations. Samples from each site include: 1.) PNG-15-70; 2.) PNG-14-19E, PNG-14-19F, and PNG-16-17D2H; 3.) PNG-14-33A and PNG-14-33B; 4.) PNG-15-50B and PNG-16-151e from adjacent sites; see Figure S6 for details. Topography from 90-m SRTM (Shuttle Radar Topography Mission) data and GeoMapApp (http://www.geomapapp.org). AUS = Australian Plate; PAC = Pacific Plate; NBP = North Bismarck Plate; SBP = South Bismarck Plate; WP = Woodlark Plate; NBT = New Britain Trench; SCT = San Cristobal Trench. MF = Mai'iu fault; GF = Gwoira fault; MS = Mt. Suckling; MD = Mt. Dayman; MM = Mt. Masasoru; OSS = Owen-Stanley Suture zone; GI = Goodenough Island; FI = Fergusson Island; NI = Normanby Island; TB = Trobriand Block; WSR = Woodlark Spreading Ridge; WB = Woodlark Basin.

1.3. Mai'iu fault rock sequence and deformation mechanisms

Little et al. (2019) details the exhumed Mai'iu fault rock sequence. Working structurally upwards and towards the most recently formed part of the sequence, this includes: a mafic mylonite zone (1 to several 10s of metres thick), a layer of foliated cataclasite-breccia (<2 m thick), an ultracataclasite layer (~40 cm thick), and mineralogically variable fault gouges immediately below the principal displacement surface of the fault (<20 cm thick; see section 3.1 for more details of this sequence). The upwardly narrowing arrangement of progressively lower-temperature fault rocks is interpreted as a time sequence of strain localization, where the higher units are more shallowly-derived and have cannibalized those underlying them (Little et al., 2019).

The mylonitic rocks are LS-tectonites that have a strong NNE-trending stretching lineation and normal-sense shear fabrics (Little et al., 2019). Pseudosection modelling of the greenschist-facies mineral assemblage (epidote, actinolite, chlorite, albite, titanite, ±quartz, ±calcite) in the mafic mylonites indicates peak metamorphic conditions of ~425±50°C and 5.9–7.2 kbar, and these rocks are inferred to have been exhumed from ~25±5 km depth (Daczko et al., 2009). Microstructural analyses of the polyphase mafic mineral assemblage indicate that Neogene and younger shearing in the mylonite zone was accomplished by diffusion-accommodated grain-boundary sliding together with syn-tectonic chlorite precipitation at temperatures >270°C (Little et al., 2019; Mizera et al., submitted). The mylonite zone was overprinted and brittlely reworked into the structurally overlying foliated cataclasites.

The foliated cataclasites host abundant pseudotachylite veins that indicate prior seismic slip on the Mai'iu fault. $^{40}Ar/^{39}Ar$ ages for two samples of such veins are ~2.2 Ma (Little et al., 2019). Given the dip-slip rate of ~10 mm/yr, these ages suggest pseudotachylite formation (i.e., seismic slip) at depths of ~10-12 km (Webber et al., 2018; Little et al., 2019). Mutually cross-cutting pseudotachylite veins, ultramylonite bands, and ductilely sheared calcite extension veins in the foliated cataclasite layer imply mixed-mode seismic and aseismic slip, and have been used to infer a peak in fault strength near the brittle-ductile transition (Little et al., 2019, Mizera et al., submitted). Such a strength peak at ~10-12 km depth approximately coincides with the up-dip end of the corridor of microseismicity that Abers et al. (2016) attribute to the Mai'iu fault at depths of 12-25 km. Gouges comprise the principal slip zone in outcrops. The gouges are not cut by veins or folded by any of the foliations present in the underlying units, suggesting that these gouges formed and slipped during latest stages of deformation in the uppermost few km of the fault zone. Overall, microstructural analyses of the Mai'iu fault rock sequence reveal that the fault zone accommodates shear strain in both seismic slip and aseismic creep via a complex synexhumational series of frictional-viscous deformation mechanisms.

2. Campaign GPS experiment

2.1. GPS data and velocities

In 2015, a network of 12 new campaign GPS monuments was installed near Mt. Dayman, ranging from the domal footwall of the Mai'iu fault northward across the fault trace into the lowlands of the hanging wall and the coast of Collingwood Bay (Figure 1d). The network was designed with densest station spacing in the lowlands to resolve any signal of elastic strain accumulation in the hanging wall of the Mai'iu fault. Stations were installed with station spacings of 3–5 km sub-parallel to fault slip direction (NNE, Figure 1d). We measured all these sites in 2015 and remeasured most of them in 2016 and 2018 using Zephyr geodetic antennas with Trimble 5700 and R7 receivers. Due to the absence of road access in the area, all of the lowland sites were visited on foot and the high mountain footwall sites were accessed via helicopter and on foot. All observations lasted at least two days, with most lasting three or more. A few of the sites were destroyed over the course of the study: URIA was destroyed between 2015–2016 (after the first measurement), and KABU and DD01 were destroyed between 2016–2018 (after the second measurement). Additionally, we remeasured seven previously established sites (Wallace et al., 2014), extending the time series of these original sites and helping tie the new sites into the pre-existing regional campaign GPS network. We incorporated campaign GPS data collected at 40 sites between 2009–2012 by Wallace et al. (2014), as well as data from a few sites measured by Australian National University prior to 2009. The sites and years of all campaign data are listed in Table S1.

Data were processed and aligned with the global reference frame ITRF14 using the GAMIT and GLOBK software packages (Herring et al., 2015, 2018). We used GAMIT to estimate orbital and rotational parameters, ionospheric and neutral atmospheric delays, and phase ambiguities to solve for the relative positions and covariance matrices of sites in our network. We also accounted for ocean tidal loading (from Onsala Space Observatory, http://holt.oso.chalmers.se/loading/) in the processing. These relative solutions were combined with solutions from global continuous GPS stations using a global Kalman filter, GLOBK, placing tight constraints on the positions of a subset of well-established global IGS network sites in order to tie our site positions into the ITRF14 reference frame. Site velocities were estimated from time series of daily position solutions. Formal uncertainties were augmented to account for random-walk noise (e.g., following approaches used by Beavan et al., 2016; Koulali et al., 2015; Williams et al., 2004; Zhang et al., 1997; see Text S1).

To correct for static coseismic displacements at our sites due to regional large earthquakes (e.g., Banerjee et al., 2005; Tregoning et al., 2013), we used STATIC1D (Pollitz, 1996) to calculate the surface displacement at each site due to static elastic interactions from planar dislocations in a spherical layered half-space with PREM elastic stratification (Dziewonski & Anderson, 1981), representing fault slip in the 2007 M_w 8.1 Solomon Islands earthquake and all M_w 6.9+ earthquakes from 2009 to July 2018 (Hayes, 2017; Lay et al., 2017; Lee et al., 2018; Strasser, 2010; Taylor et al., 2008; U.S. Geological Survey, 2019; Wallace et al., 2015). These regional earthquakes were between 350 and 825 km away from our local network spanning the Mai'iu fault. See Text S2 for details.

Relative to a fixed Australian Plate, horizontal velocities for sites on the hanging wall of the Mai'iu fault trend NNE, approximately perpendicular to the fault trace. These velocities generally align with previously reported velocities showing southeast PNG rotating counterclockwise relative to the Australian Plate around a nearby Euler pole (Figures 1, 2; Wallace et al., 2014). Hanging-wall velocities gradually increase with strike-perpendicular distance northwards from the fault trace and show 8.3±1.2 mm/yr of NNE-SSW horizontal extension across the fault, corresponding to 7.6-10.2 mm/yr dip-slip rates for a 21°-dipping fault. One outlier is the hanging wall site nearest to the fault trace, YAMS, which shows subtle NNW motion.

2.2. Elastic block and dislocation modeling approaches

We undertake two different approaches to modeling the GPS velocity data to investigate the degree of interseismic coupling and slip rates on the Mai'iu fault. To tie our velocities into a regionally kinematically consistent reference frame, we first use an elastic block modeling approach (similar to Wallace et al., 2014). After establishing a fixed-footwall reference frame using the elastic block model, we use simpler two-dimensional elastic dislocation models to determine the Mai'iu fault properties that best explained the observed surface velocity data (similar to Hreinsdóttir & Bennett, 2009).

In the elastic block models, we represent the tectonic deformation responsible for GPS velocities in southeast PNG as the interactions between adjacent elastic crustal blocks, with each rotating about an independent Euler pole of rotation. Although we are most interested in near-field deformation associated with the Mai'iu fault, our wider dataset spans the broader southeast PNG region where crustal deformation can be described by the rotations and interactions between numerous microplates and crustal blocks (Wallace et al., 2014; Figures 1, 2a). Therefore, we model multiple crustal blocks (Figure 2a) and invert the GPS velocities for poles of rotation for each block relative to the Australian Plate (our velocities are in an Australia-fixed reference frame).

In these crustal block models, elastic strains accumulated along block boundaries are modeled as backslip on block-bounding faults and parameterized by the kinematic fault coupling ratio, Φ, which describes the fraction of predicted relative plate motion that is accrued as a slip deficit rate. For example, if $\Phi = 0$, the fault is creeping at full plate motion rate, while if $\Phi = 1$, there is no creep in the interseismic period of our GPS measurements and the fault is fully locked. The slip deficit rate is simply the coupling ratio multiplied by the long-term slip rate on the fault from the crustal block motions. We use TDEFNODE (McCaffrey, 2002) to jointly invert for the block poles of rotation and the spatial distribution of Φ on block-bounding faults. The model is constrained by kinematic data including GPS velocities, earthquake slip vectors, and transform fault orientations from throughout the southeast PNG region.

Block boundaries and fault geometries are defined on the basis of regional tectonics, field mapping studies, and geophysical constraints such as seismicity. For this model, block and fault geometries are based largely on those of Wallace et al. (2014), although some geometries such as the position and dips of the Mai'iu fault have been updated based on recent field mapping (Little et al., 2019; Mizera et al., 2019; Webber et al., 2018, 2020) and seismological observations (Abers et al., 2016). The statistical significance of various block configurations is tested with an *F*-test for block independence (Figures 2a, S3; Table S5). We utilize our preferred configuration for subsequent models testing fault coupling (Figure 2a).

Joint inversion of diverse local and regional kinematic datasets within a block model framework helps to ensure that modeled block rotations and fault coupling are consistent with both regional tectonic motions and local observations. In addition, simple 2-D planar dislocation fault models can provide focused insight into the tradeoffs between slip rate, locking depth, and fault geometry, especially for dense GPS networks that span major active faults. For this reason, we also perform a simple inversion of strike-perpendicular GPS velocities across the Mai'iu fault for fault dip, locking depth, and dip-slip rate using the solutions for planar dislocations in an elastic half-space from Okada (1985). This simplified 2-D approach has been used to model GPS velocities related to slip on other LANFs (Hreinsdóttir & Bennett, 2009) and reverse and strike-slip faults (Beavan et al., 1999). In such models, a single fault is represented as a two-dimensional planar dislocation that extends infinitely in the third dimension. In our case, predicted elastic contributions to surface displacement due to interseismic backslip on the locked dislocations are added to the long-term fault-strike-perpendicular plate motion rate and compared with observed surface velocities to calculate the misfit between the model and the data. By minimizing the data misfit as expressed by the reduced χ^2, these models highlight the range of fault properties and locking most likely responsible for observed surface displacements. The calculated χ^2 is minimized through an extensive grid search of the three fault parameters (dip, slip rate, and locking distribution), as discussed in Section 3.2.

2.3. Elastic block model results

Our preferred elastic block model treats Fergusson/Goodenough Islands, Normanby Island, Goodenough Bay, and the Papuan Peninsula as discrete independent crustal blocks, similar to that of Wallace et al. (2014). More complex configurations (with additional blocks) do not produce a statistically significant improvement in fit to the data (see *F*-tests and results in Figures 2a, S3; Table S5). The best-fitting model of jointly inverted block poles of rotation and fault locking are shown in Figure 2a, indicating 8.3±1.2 mm/yr of horizontal extension across the Mai'iu fault. This model predicts locking of the western segment of the Mai'iu fault down to only 2 km depth, below which the fault creeps. Deeper locking occurs on the eastern segment through Goodenough Bay and the faults immediately north of Goodenough Island, although this is not well-constrained due to a relative lack of GPS sites on the largely submarine hanging-wall east of our study area.

Inversions producing the model in Figure 2 allow fault coupling ratios to vary from 0 – 1, but they impose a constraint that coupling decreases with increasing depth. To test how such assumptions affect the preferred locking model, additional inversions were performed with different constraints on locking, such as allowing coupling to vary freely with depth or assuming a discrete and uniform locking depth (Text S3; Figure S4). The large misfit of models with prescribed locking depths from the surface to >~2 km confirm that campaign GPS velocities are inconsistent with Mai'iu fault locking from the surface to more than a few kms depth. Inversions with fewer imposed locking constraints, including those in which no downdip decrease in coupling is prescribed (i.e., no assumption that the fault is locked at the surface), all converge on best-fitting models with shallow locking to <2 km depth (Figure S4), compatible with a LANF creeping at most depths.

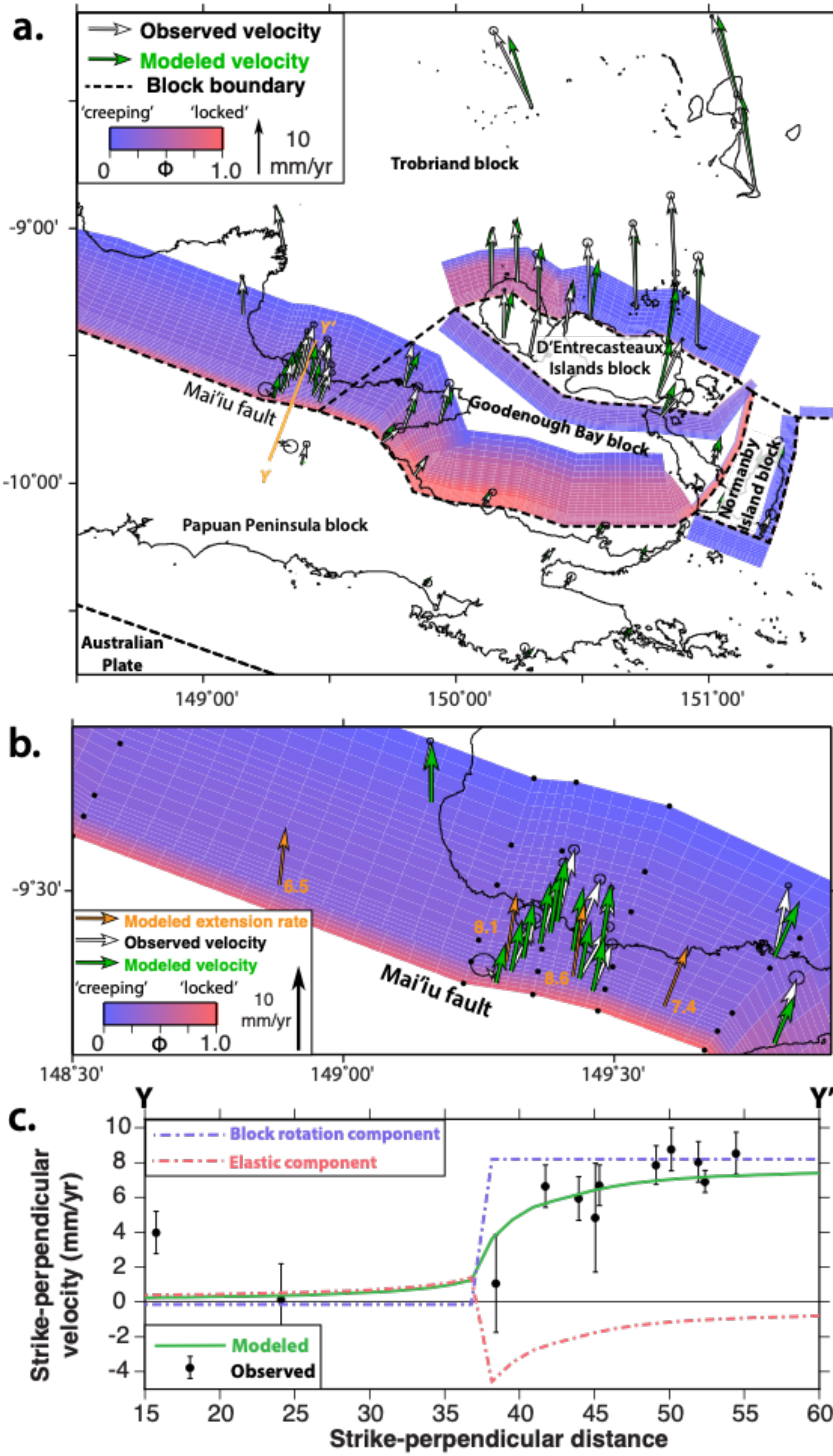

a.
Observed velocity
Modeled velocity
Block boundary
'creeping'
'locked'
0
Φ
1.0
10 mm/yr
Trobriand block
D'Entrecasteaux Islands block
Goodenough Bay block
Normanby Island block
Mai'iu fault
Y'
Y
Papuan Peninsula block
Australian Plate
-9°00'
-10°00'
149°00'
150°00'
151°00'
b.
6.5
8.1
8.6
7.4
Modeled extension rate
Observed velocity
Modeled velocity
'creeping'
'locked'
10 mm/yr
0
Φ
1.0
Mai'iu fault
-9°30'
148°30'
149°00'
149°30'
c.
Y
Y'
Block rotation component
Elastic component
Modeled
Observed
Strike-perpendicular velocity (mm/yr)
Strike-perpendicular distance
10
8
6
4
2
0
-2
-4
15
20
25
30
35
40
45
50
55
60

383

Figure 2. Best-fitting elastic block fault locking model results colored by kinematic fault coupling ratio Φ. Vectors indicate observed (white) and predicted (green) GPS velocities. a.) Preferred locking model. Dashed lines show preferred block boundaries (Figure S3; Table S3). b.) Enlarged view of GPS velocities near the modeled Mai'iu fault, which is predominantly uncoupled below 2 km depth. Labeled orange vectors show modeled rates and directions of relative motion between adjacent blocks across the fault. c.) Strike-perpendicular horizontal velocities relative to the Papuan Peninsula footwall block for sites in the Mai'iu fault network (Profile Y – Y' in 2a). Observed velocities (black), modeled velocities (green), and the modeled velocity contribution of elastic strain (pink) and block rotations (purple) are shown.

2.4. 2-D Dislocation modeling

2.4.1. Model 1: Locked-to-surface models

Modeled crustal block rotations help to establish a footwall-fixed reference frame in which explore Mai'iu fault locking in more detail using 2D dislocation models. We compare the predicted horizontal surface velocities (now in a footwall-fixed reference frame) from 128,000 two-dimensional elastic half-space planar dislocation models to the strike-perpendicular GPS velocities from sites within a 65 km strike-perpendicular distance of the Mai'iu fault trace along profile X-X' (Figure 1b). This approach offers a focused look at how modeled fault properties affect the fit to GPS velocities, but does not account for three-dimensional factors such as along-strike variations in fault geometry or locking. We first test the slip rate, dip angle, and locking depth of a single fault locked to the Earth's surface, as in previous GPS studies of LANF locking (Hreinsdóttir & Bennett, 2009). Although the shallow (≤24°) dip of the Mai'iu fault along its trace is well-constrained (Little et al., 2019; Mizera et al., 2019), the fault surface exhumed on the Dayman-Suckling metamorphic core complex steepens northward (Webber et al., 2020), and fault-related microseismicity implies a similar northward steepening dip (Abers et al., 2016). We therefore allow the modeled fault dip to vary in order to more fully explore the parameter space. We test fault dip angles ranging from 1 - 80° in 1° increments, dip-slip rates of 0.5 – 20 mm/yr in 0.5 mm/yr increments, and locking depths of 0.5 – 20 km in 0.5 km increments (Figures 4a, S6). For the strike-perpendicular horizontal velocities, the best-fitting (minimum $\chi^2 = 0.94$) modeled fault dips 26°, is locked down to 2 km depth, and slips at 10 mm/yr below this depth (model 1; Figure 3a-c). This result indicates that the observed GPS horizontal velocities can be explained by active aseismic creep below a shallow locking depth on a gently dipping normal fault. The close match between the best-fit model's fault dip and the geologically inferred fault dip supports this result. Vertical velocities (which have high uncertainties) are modeled (Figure 3b,e) but not used to constrain the grid search. Joint modeling of vertical and horizontal components (e.g., Beavan et al., 2010; Bennett et al., 2007; Segall, 2010; Serpelloni et al., 2013) yields similar locking results (Text S4). Note that the best-fit $\chi^2 < 1.0$ suggests that the random-walk noise model may slightly overestimate the velocity uncertainty corrections, particularly for campaign sites with only two or three years of observations.

2.4.2. Model 2: Consideration of shallow creep and splay fault activity

The setup of model 1 is inherently limited by the assumptions that the fault is locked at the surface and that only one planar structure is active, which may not be appropriate for this and other LANF systems. The hanging walls of major detachment faults are commonly cut by minor splay faults that may variably slip or creep (e.g., Anderlini et al., 2016). In the case of the Mai'iu fault, discontinuous splay faults have been mapped in parts of the hanging wall (Figure 1b; Little et al., 2019, Webber et al., 2020). Additionally, the shallow portions of many LANFs, including the Mai'iu Fault (section 3.2-3.3), contain gouges of weak, frictionally stable mineralogies that may promote near-surface aseismic creep (Collettini, 2011, and references within; Little et al., 2019). To test whether these mechanisms allow aseismic creep in the near-surface portions of the Mai'iu fault and/or its splay faults, we develop buried dislocation models that do not require full fault locking at the Earth's surface and that allow for slip on adjacent splay faults (model 2).

Our buried dislocation models allow for creep both updip and downdip of a locked patch or "asperity" (e.g., Collettini et al., 2019). Because the velocity at YAMS is more consistent with footwall motion, we treat it as a footwall site in these models: essentially, this treatment considers the possibility that, in the shallowest subsurface, creep may transfer from the main Mai'iu fault to one of the many active splay faults in the hanging wall, some of which are <1 km from the main fault trace (Little et al., 2019). The modeled fault trace is hence projected between sites YAMS and BINI in order to incorporate YAMS into the footwall. Note that in all dislocation models, including both locked-to-surface and buried dislocation scenarios, the data-fit improves significantly by treating site YAMS as part of the footwall. The best-fit buried dislocation model (model 2; $\chi^2 = 0.89$; Figure 3d-f) fits the horizontal velocities better than the best-fit model with locking imposed at the surface (model 1; $\chi^2 = 0.94$; Figure 3a-c). The best-fit model with a buried locked zone involves a 35°-dipping fault, locked from 5 to 16 km depth and slipping at 10.5 mm/yr updip and downdip of the locked zone (Figure 3d-f), consistent with microseismic, structural, and surface modeling evidence that the Mai'iu fault steepens to dip 30-40° between ~5-12 km depth (Abers et al., 2016; Little et al., 2019; Webber et al., 2020). Fixing fault dip to a geologically and geodetically reasonable average crustal dip of 35°, Figure 4b shows tradeoffs between the total depth range of locking (depth range D, Figure 3f), the depth of the updip limit of locking (depth P, Figure 3f), and slip rate.

Model 2 assumes that interseismic fault creep updip of a more strongly locked region is mechanically feasible. Shallow interseismic fault creep occurs above locked seismogenic patches on a variety of faults (Harris et al., 2017), including the strike-slip Hayward fault in California (Harris et al., 2017 and references within) and the Nankai subduction megathrust, where periodic slow-slip events near the trench occur updip of the locked portion of the megathrust (Araki et al., 2017). However, recent analytical models predict a strong stress-shadow effect updip of the locked portion of subduction megathrusts that should prevent significant creep on the unlocked updip portion of the fault regardless of its frictional stability (Almeida et al., 2018). In other words, even an unlocked, frictionally stable shallow portion of a megathrust may not feel high enough driving stresses to creep interseismically when located updip of a strongly locked patch. By analogy, this type of model may predict that significant shallow creep updip of a more strongly locked portion of a LANF should not occur, either.

Because the downdip width (~19 km) of the locked LANF patch inferred by model 2 is much smaller than that of a locked megathrust, and because along-strike locking patterns may be heterogeneous and patchy, the efficacy of this stress shadow effect may be limited. Additionally, the stress shadow models (Almeida et al., 2018) assume homogeneous elastic properties at all depths, whereas the shallow portions of many normal fault hanging walls consist of unconsolidated, fractured sedimentary units. High shear stresses associated with deep creep between strong metabasaltic and plutonic rocks could be expected to drive more internal deformation and/or fault creep in weak hanging wall sediments at shallow levels than in the strong hanging wall of the homogeneous model. Heterogeneous locking and elastic properties along with frictionally weak, velocity-strengthening shallow fault gouges (section 3) help explain how shallow interseismic creep coeval with deeper locking (model 2) is a mechanically feasible model for interseismic LANF slip.

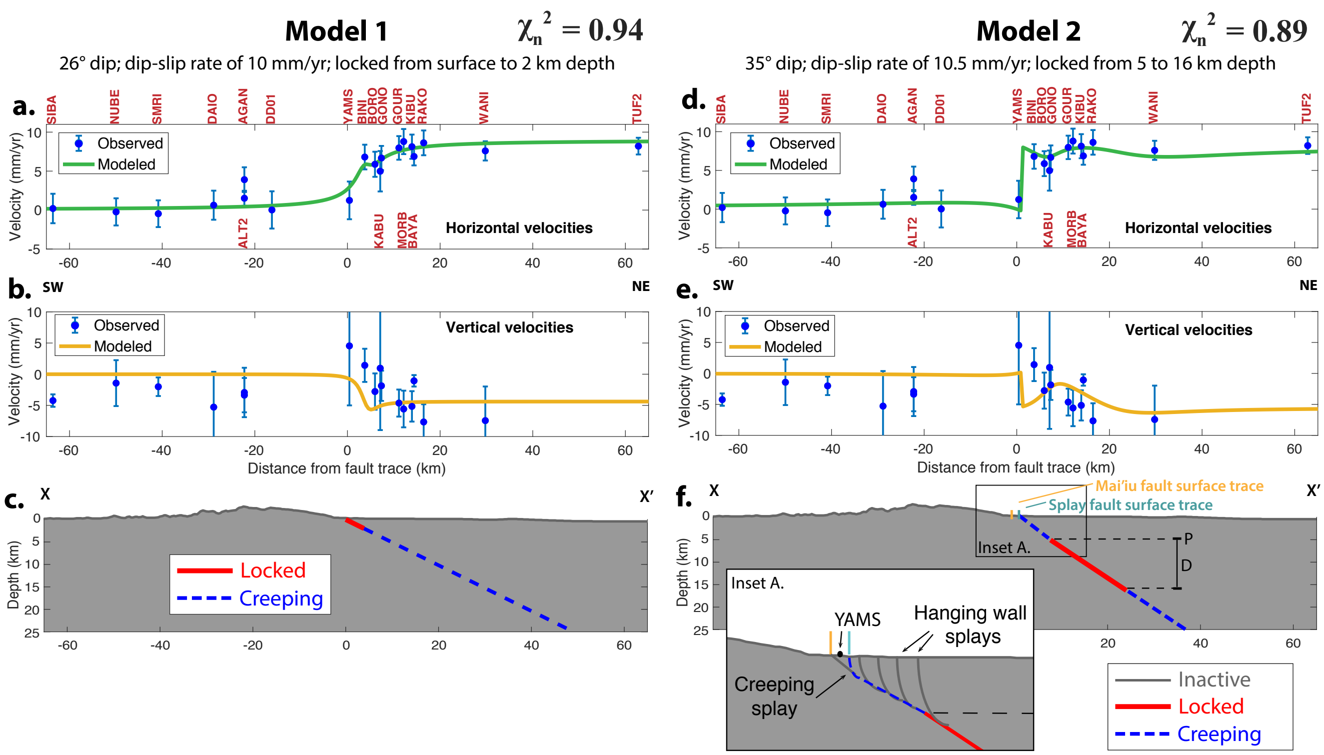

Figure 3. Best-fitting two-dimensional planar elastic half-space dislocation locking models based on strike-perpendicular horizontal velocities projected onto profile X-X' of Figure 1b. Red labels show GPS site names. a-c.) Model 1; locked to 2 km depth. d-f.) Model 2; locked from 5 to 16 km depth, with creep and splay fault slip above 5 km depth. a,d): Observed (blue) and modeled strike-perpendicular velocities. b,e): Observed and modeled vertical velocities. c,f): Schematic of fault locking models. Profile topography from 90-m SRTM data and GeoMapApp (http://www.geomapapp.org).

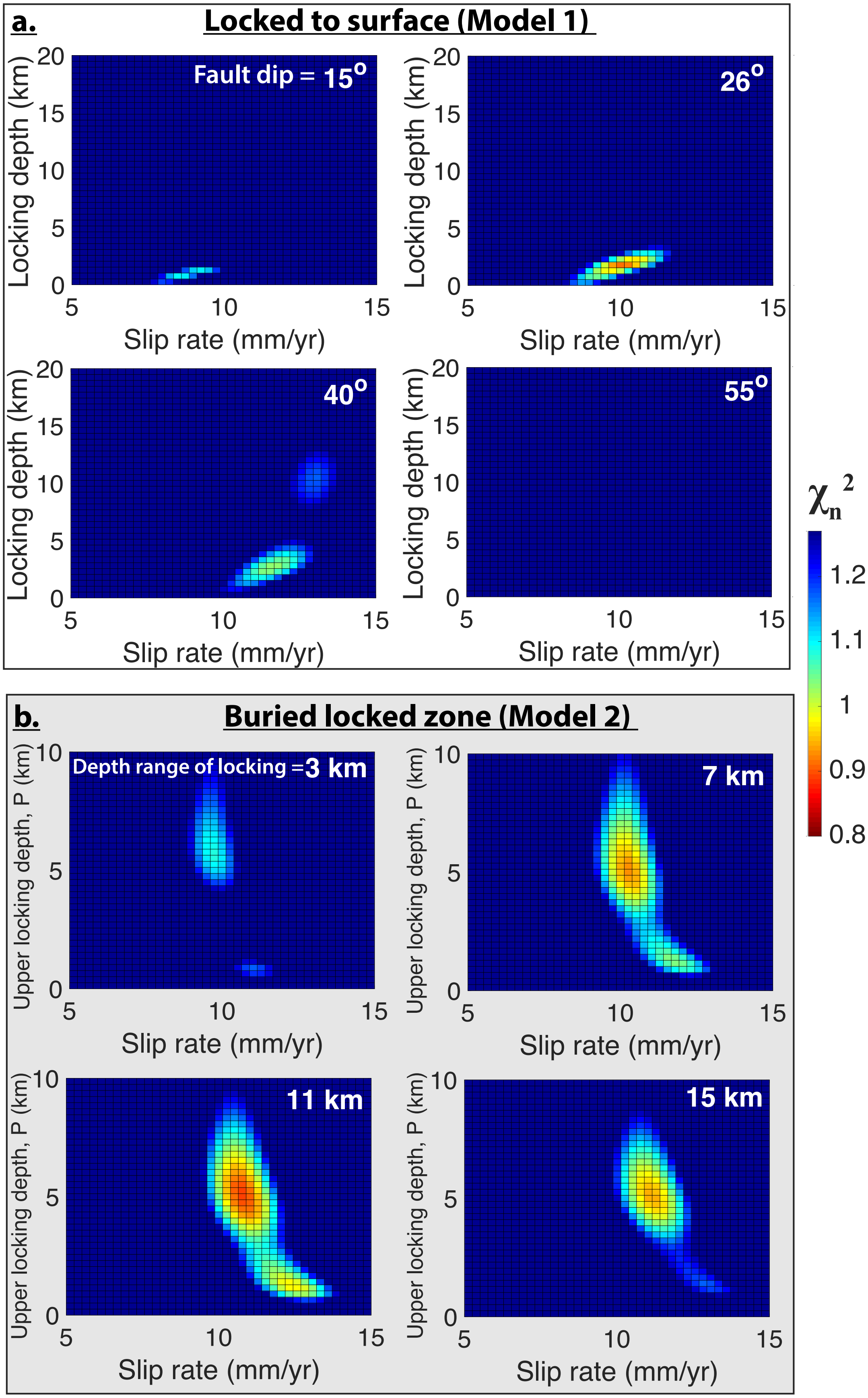
a.
Locked to surface (Model 1)
Fault dip = 15°
26°
40°
55°
Locking depth (km)
Slip rate (mm/yr)
b.
Buried locked zone (Model 2)
Depth range of locking =3 km
7 km
11 km
15 km
Upper locking depth, P (km)
Slip rate (mm/yr)
χ_n^2
1.2
1.1
1
0.9
0.8

Figure 4. Example of misfit (χ^2) tradeoffs for 2D dislocation models capped at χ^2=1.27 (equivalent to 75% confidence interval for model 2 calculated with *F*-tests for statistical significance) to highlight those models that fit the data reasonably well. a.) Tradeoffs between locking depth and slip rate for locked from surface to depth models with different dip angles. Locked-at-surface models prefer shallow locking (<4 km depth) on a shallowly dipping (~26°) fault slipping ~9-12 mm/yr, while steeply dipping faults (≥ 40°) do not fit the data well (χ^2 > 1.0). b.) Buried-dislocation models show tradeoffs between the updip depth of locking (depth P, Figure 3f) and slip rate with different depth ranges of locking (depth D, Figure 3f). Fault dip shown here is fixed to the best-fitting value of 35°; however, P, D, slip rate, and dip were all varied in grid searches. These models prefer a more strongly locked zone from ~5-16 km depth on a shallowly dipping (~35°) fault slipping ~10-12 mm/yr.

3. Mai'iu fault frictional strength and stability from rock deformation experiments

3.1. Fault rock sample descriptions

Over three field seasons, spectacular exposures of the Mai'iu fault were observed and sampled. Structural results show that fault slip has occurred primarily within fault rocks comprising a narrow (< 3 m), high strain fault core (Little et al., 2019) (Figure 5). The frictional properties of these fault rocks likely govern the mode of frictional fault slip at different levels on the fault. Figure 5b shows a schematic section of the Mai'iu fault rock sequence that is partially eroded on exhumed parts of the active fault, but fully preserved in outcrops along the inactive segment of the Mai'iu fault. Eight Mai'iu fault rock samples were studied in detail to determine their mineralogy and frictional properties: two types of footwall foliated cataclasite (Figure 5c); a footwall ultracataclasite (Figure 5d); four types of footwall fault gouge (Figures 5e and 5f); and a sliver of hanging wall serpentine schist entrained within the footwall (Figure 5c, inset).

The mylonitic rocks (not sampled for friction experiments) were overprinted and reworked into the structurally overlying, ~2 m-thick foliated cataclasites. The latter contains veins of friction melt (pseudotachylite), brittle faults, and multiple generations of calcite veins (Figure 5c). The foliated cataclasites investigated in this study (PNG16-17-D2H and PNG16-151E) have a cm-to-mm-spaced, differentiated, and pervasively folded foliation defined by light-coloured albite and quartz±calcite-rich domains and darker phyllosilicate (predominantly chlorite)-rich folia. This microstructure indicates fluid-assisted diffusive mass transfer during the dissolution of mafic minerals (epidote and actinolite) (Mizera et al., submitted). Shear-induced creep by diffusive mass transfer and/or frictional viscous flow likely accompanied the formation and folding of the pervasive foliation (Little et al., 2019; Mizera et al., submitted).

In all outcrops, the foliated cataclasites are overlain sharply by a 5-to-40 cm-thick ultracataclasite (PNG15-50B) formed through cataclastic grain-size reduction and authigenic precipitation of calcite, corrensite, and potassium feldspar (Figure 5d). Massive green-gray and red mafic gouges (PNG14-33A and PNG14-33B) or light (PNG14-19E) to medium grey (PNG14-19F) corrensite-saponite gouges sharply overly the ultracataclasite layer and form the <20 cm-thick principal slip zone in surface outcrops (Figures 5a, 5b, 5e and 5f).

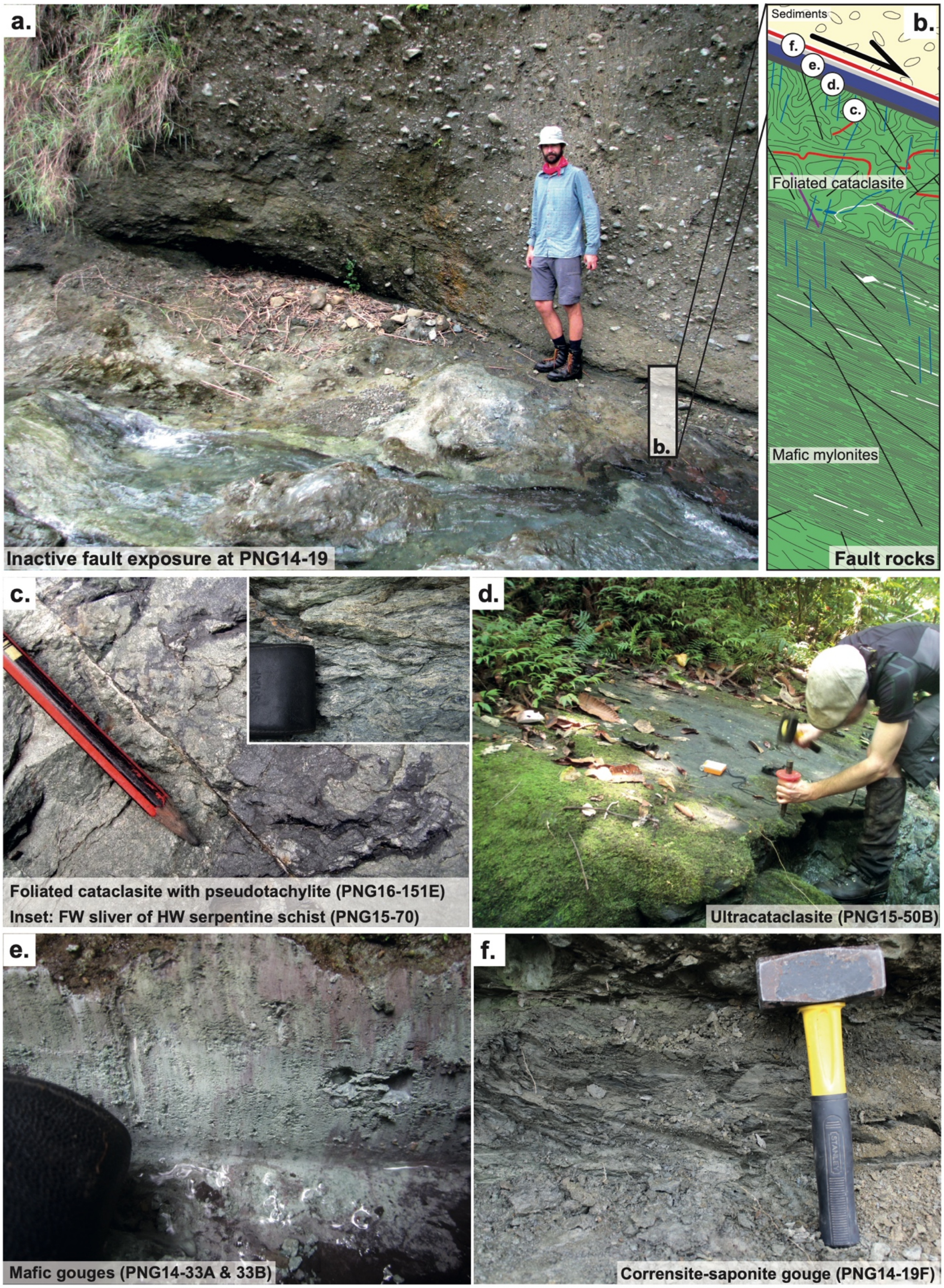
a.
Inactive fault exposure at PNG14-19
b.
Sediments
b.
f.
e.
d.
c.
Foliated cataclasite
Mafic mylonites
Fault rocks
c.
Foliated cataclasite with pseudotachylite (PNG16-151E)
Inset: FW sliver of HW serpentine schist (PNG15-70)
d.
Ultracataclasite (PNG15-50B)
e.
Mafic gouges (PNG14-33A & 33B)
f.
Corrensite-saponite gouge (PNG14-19F)

533

Figure 5. Summary of fault rocks analyzed. Sample locations are shown in Figures 1d and S7 and listed in Table S6. (a) Exposure of the inactive Mai'iu fault showing the footwall fault rock sequence sharply overlain by unmetamorphosed hanging wall sedimentary rocks. (b) A schematic cross section through the fault core, including the structural position of the fault rocks sampled (after Little et al., 2019; Mizera et al., submitted). (c) Fault-exhumed exposure of the foliated cataclasite unit and a pseudotachylite vein. Inset: foliated serpentine schist (>10 m thick) entrained between the footwall and hanging wall of the Mai'iu fault, stranded atop the footwall north of Mt. Masasoru. (d) Outcrop of cohesive ultracataclasite unit structurally overlying foliated cataclasites. (e) Mafic fault gouges, and (f) corrensite-saponite fault gouge comprising the principal slip zone.

3.2. Experimental methods and materials

We performed hydrothermal friction experiments on powdered gouges derived from eight of these Mai'iu fault rock types (Figure 6; Table S6-7) using the rotary shear apparatus in the High Pressure and Temperature Laboratory at Utrecht University (Niemeijer et al, 2008, 2016). In these experiments, a thin layer (~1.5 mm) of gouge is placed between two ring-shaped Ni-alloy pistons (22/28 mm inside/outside diameter) and confined by Ni-alloy rings with a low friction (Molykote) coating. The piston assembly is mounted inside a water-filled pressure vessel that houses an internal furnace. The vessel is located within a 100 kN capacity Instron loading frame which is used to apply the normal force. Rotation of the vessel creating shear within the layer is achieved using an electromotor attached to two 1:100 gear boxes. For more details, refer to Niemeijer et al (2008, 2016).

To create a powdered gouge, samples were crushed and sieved to a grain size fraction < 150 μm. In all experiments, we applied stepwise increases in effective normal stress (15 MPa/km), fluid pressure (10 MPa/km) and temperature (25 °C/km) to simulate slip in progressively deeper parts of the fault (Table S5). Once the desired pressure (P) and temperature (T) conditions were reached, we allowed the system to equilibrate for at least 30 minutes before shearing began at 1 μm/s. Initial shearing at 1 μm/s occurred for 5 mm to establish a steady state friction level and a mature microstructure. The velocity dependence of friction was investigated by subsequently applying a velocity-stepping scheme of 0.3-1-3-10-30 μm/s. Following these velocity steps, the motor driving displacement was stopped, and PT conditions were changed. Under the new PT-conditions, the 1 μm/s run-in displacement was reduced to 2.5 mm, but otherwise the procedure remained the same. Data were acquired at a rate of 900 Hz and averaged to rates of 1-100 Hz, depending on the sliding velocity. Raw data were processed to obtain shear stress as a function of sliding distance, which was further analyzed in terms of rate-and-state frictional (RSF) properties using a Dieterich state evolution law (Dieterich 1979, 1981; Marone, 1998) and the inversion scheme detailed in Reinen & Weeks (1993) and.

3.3. Frictional strength results

We report the results of all experiments in Figure 6, which shows the coefficient of friction (defined as shear stress / effective normal stress, ignoring cohesion) as a function of load-point displacement. All samples tested show changes in friction with PT conditions, but the largest differences in friction are between samples. The measured frictional strength covers the range of μ=0.1 to μ=0.8 (see also Table S7 and Text S5). The uppermost, light gray saponite gouge sample is the weakest with μ=0.11-0.15, followed by the underlying, medium gray saponite gouge (μ=0.18-0.28), the red mafic gouge (μ=0.22-0.35), the serpentinite schist (μ=0.37-0.63), the green-grey mafic gouge (μ=0.40-0.57), the “inactive” foliated cataclasite (0.44-0.75), the “active” foliated cataclasite (μ=0.57-0.67) and finally the ultracataclasite (μ=0.59-0.80). The abundance of the weak clay mineral saponite is a good indicator of the weakness of the sample (e.g. Lockner et al., 2011; Sone et al., 2012), whereas the sample derived from the serpentinite schists show friction values in the range of pure lizardite (e.g. Reinen et al., 1994; Behnsen & Faulkner, 2012). Friction of the foliated cataclasites and the ultracataclasite is comparable to results from friction studies on gouges of granitic composition (e.g. Niemeijer et al., 2016), of quartz (e.g. Chester & Higgs, 1992; Niemeijer et al., 2008), and of plagioclase (e.g. He et al., 2013). In general, the friction coefficients of most fault gouges increase with increasing simulated depth (i.e., increasing temperature, effective normal stress, and fluid pressure) during an individual experiment. In some experiments, strengthening is the result of a long-term displacement-dependent increase in friction (e.g. Figure 6c), whereas in other experiments strengthening is abrupt and is the result of increased simulated depth (e.g. Figure 6b).

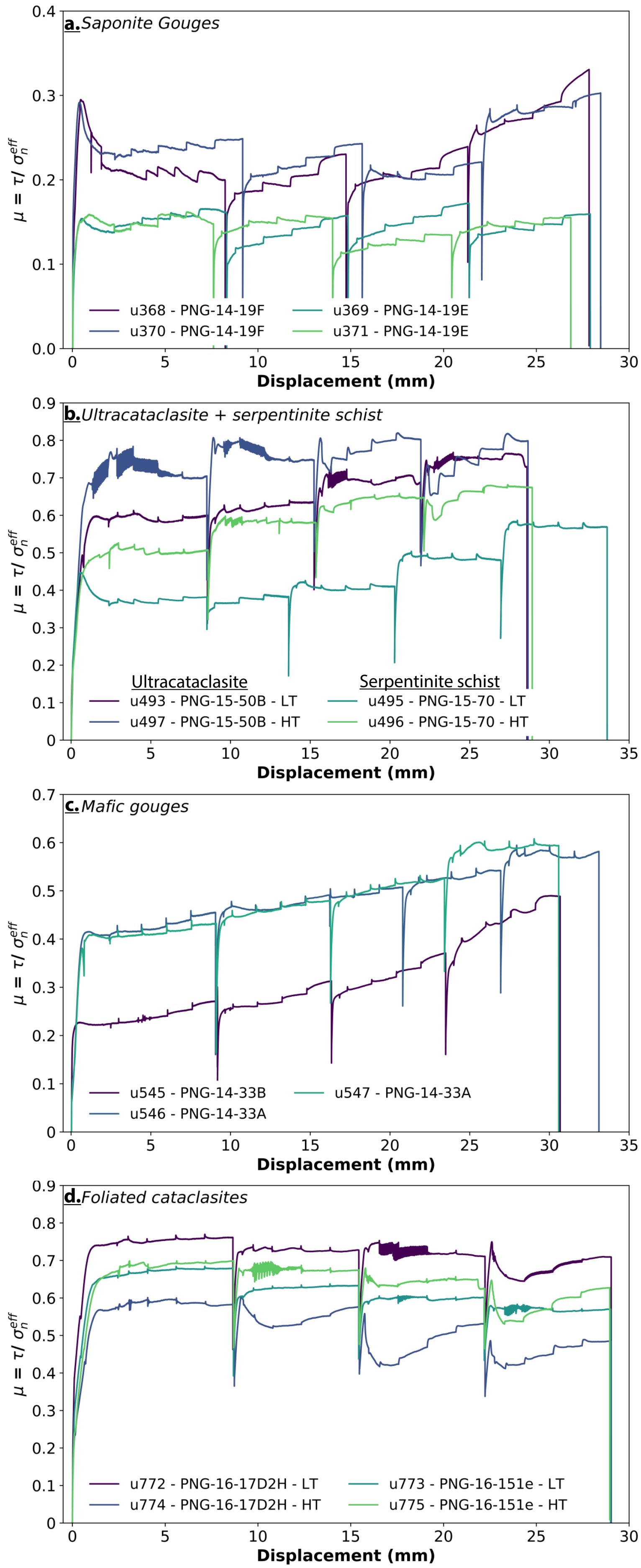

a. Saponite Gouges
u368 - PNG-14-19F
u369 - PNG-14-19E
u370 - PNG-14-19F
u371 - PNG-14-19E
Displacement (mm)
$\mu = \tau / \sigma_n^{eff}$
b. Ultracataclasite + serpentinite schist
Ultracataclasite
u493 - PNG-15-50B - LT
u497 - PNG-15-50B - HT
Serpentinite schist
u495 - PNG-15-70 - LT
u496 - PNG-15-70 - HT
Displacement (mm)
c. Mafic gouges
u545 - PNG-14-33B
u546 - PNG-14-33A
u547 - PNG-14-33A
Displacement (mm)
d. Foliated cataclasites
u772 - PNG-16-17D2H - LT
u774 - PNG-16-17D2H - HT
u773 - PNG-16-151e - LT
u775 - PNG-16-151e - HT
Displacement (mm)

595

Figure 6. Friction measured during velocity-step experiments on Mai'iu fault rocks (Section 3.1, Figure 5, Table S6-7) including a.) corrensite-saponite gouges, b.) ultracataclasite and serpentinite schist; c.) mafic gouges; d.) foliated cataclasites. Colors indicate individual experiments ('u368') on numbered samples ('PNG-14-19F') under lower-temperature (LT) or higher-temperature (HT) conditions.

3.4. Rate-and-state frictional stability results

Although a relationship between fault strength and frictional stability has been proposed (Ikari et al., 2011), fault frictional strength alone gives little indication as to whether the fault creeps aseismically or slips in episodic earthquakes. Instead, frictional stability is described within the framework of rate-and-state friction, where the instantaneous effective friction coefficient depends on both the current slip velocity ('rate') and the time over which two fault surfaces have been in contact with each other ('state'). Experimentally derived values of rate-state parameters a, b, and critical slip distance d_c describe the frictional stability of a material: materials with $(a–b)>0$ are velocity-strengthening, whereby an increase in slip velocity causes an increase in friction promoting stable creep; materials with $(a–b)<0$ are velocity-weakening, whereby an increase in slip velocity causes a decrease in friction, promoting unstable, potentially seismic slip (e.g., Dieterich, 1979, 1981; Gu et al., 1984; Rice & Tse, 1986; Ruina, 1983).

We invert the velocity-stepping data for individual rate-state friction parameters a, b and d_c. Figure 7 shows $(a–b)$ values as a function of up-step sliding velocity for all samples tested. There is considerable variation in $(a–b)$ with simulated depth. All samples show some negative $(a–b)$ values under certain experimental conditions, indicating potential for unstable slip. In all fault gouge-derived samples, $(a–b)$ increases with increasing sliding velocity, regardless of the depth simulated (Figures 7a, 7c). Negative values are restricted to temperatures of 150-200 °C. Samples derived from foliated cataclasites and ultracataclasites show predominantly negative values of $(a–b)$ transitioning to positive values at temperatures of 400 and 450 °C. Interestingly, at these temperatures $(a–b)$ decreases with increasing sliding velocity. Finally, $(a-b)$ values for the sample derived from serpentinite schist show three regimes of velocity dependence, similar to the results of Reinen et al. (1994): low temperature (<200 °C) velocity strengthening, intermediate temperature (200-350 °C) velocity weakening and high temperature velocity strengthening (400-450 °C). As before, $(a–b)$ decreases with increasing sliding velocity in the higher-temperature regime.

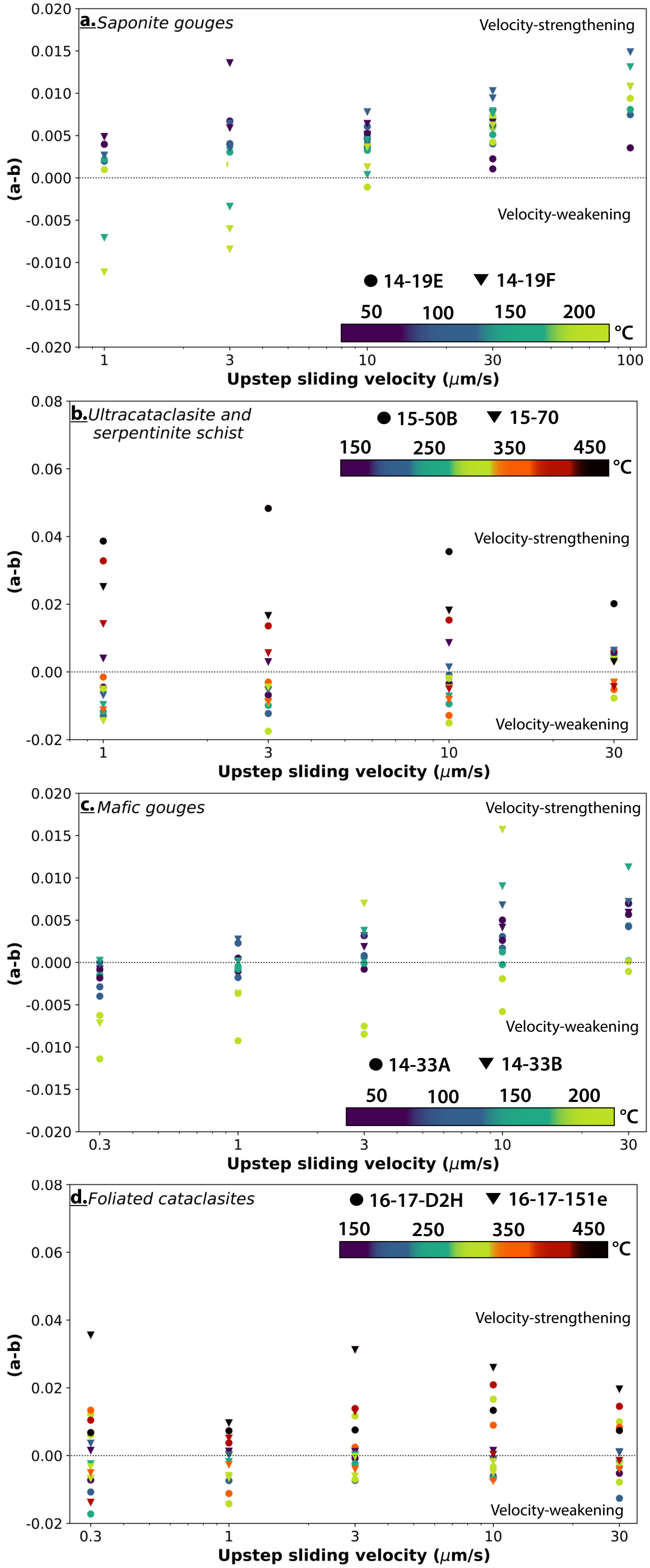

a. Saponite gouges
Velocity-strengthening
Velocity-weakening
14-19E
14-19F
50 100 150 200 °C
(a-b)
Upstep sliding velocity (μm/s)
b. Ultracataclasite and serpentinite schist
15-50B
15-70
150 250 350 450 °C
Velocity-strengthening
Velocity-weakening
(a-b)
Upstep sliding velocity (μm/s)
c. Mafic gouges
Velocity-strengthening
Velocity-weakening
14-33A
14-33B
50 100 150 200 °C
(a-b)
Upstep sliding velocity (μm/s)
d. Foliated cataclasites
16-17-D2H
16-17-151e
150 250 350 450 °C
Velocity-strengthening
Velocity-weakening
(a-b)
Upstep sliding velocity (μm/s)

630

Figure 7. Rate-state-friction stability parameters *(a-b)* from velocity-stepping experiments on Mai'iu fault rocks (Section 3.1, Figure 5, Table S6-7) including a.) corrensite-saponite gouges, b.) ultracataclasite and serpentinite schist; c.) mafic gouges; d.) foliated cataclasites.

4. Discussion

4.1. Experimental constraints on fault slip behavior

4.1.1. Evidence for frictional strain-weakening of a rolling-hinge detachment

Our experimental results show that the Mai'iu fault gouges inferred to be active at the shallowest depths are frictionally weak (μ = 0.11 – 0.35), with the most phyllosilicate-rich (saponitic) gouge exhibiting the lowest static friction coefficients of 0.11 – 0.15. Saponite is thermodynamically unstable above ~150 °C (e.g., Boulton et al., 2018; Moore, 2014), implying that these weak gouges control the frictional strength of only the shallowest and most mechanically misaligned portions of the Mai'iu fault, down to inferred depths of ~6 km (Figure 8; Mizera et al., submitted). At greater depths and higher temperatures (T = 150 – 225 and 150 – 300 °C, respectively), chlorite thermometry from syntectonic structures (e.g., veins, shear bands) indicates that slip occurred in the mafic ultracataclasite and foliated cataclasite units (Mizera et al., submitted), which are frictionally stronger (μ = 0.59 – 0.80 and μ = 0.44 – 0.75, respectively). This increase in frictional strength with depth coincides with the depth range over which the fault dip steepens from 15–22° in the upper 4–5 km to 30–40° below 5–6 km (Abers et al., 2016; Little et al., 2019; Mizera et al., 2019; Webber et al., 2020). Based on these observations, we infer that the static frictional strength of the Mai'iu fault partially controls its geometry, with slip at shallow dip angles in the near-surface facilitated by abundant weak saponitic gouges, and slip at steeper dip angles at greater depths occurring on frictionally stronger (ultra-)cataclasites, Formation of saponite (or other weak phyllosilicate minerals in other LANFs) results in a syn-exhumational reaction-weakening of the fault, consistent with classic geodynamic models of detachment faults that require plastic strain-weakening of the normal fault zone in order for it to evolve into a long-lived rolling hinge-style detachment (e.g., Lavier et al., 1999; 2000). Although this geodynamic plastic strain-weakening is commonly modeled as a loss of cohesion (e.g., Lavier et al., 1999; 2000; Choi et al., 2012; Choi & Buck, 2013), our experimental results show that the effective strain-weakening of an active rolling-hinge detachment fault (Mizera et al., 2019; Little et al., 2019) can be at least partially accomplished by the reduction of the static coefficient of friction as a result of fluid-assisted mineral transformation reactions that form weak phyllosilicate minerals such as saponite.

The static frictional strength of active LANFs is thought to influence both fault geometry according to classical Mohr-Coulomb-type fault mechanics (e.g., Axen, 2004; Choi & Buck, 2012; Choi et al., 2013; Collettini et al., 2009b; Collettini & Sibson, 2001; Yuan et al., 2020) and wedge geometry according to critical wedge theory and limit analysis (e.g., Yuan et al., 2020). The low frictional strength ($\mu \sim 0.2$) of clay-rich and/or hydrated gouge minerals such as talc and smectite should allow normal faults filled with these minerals to remain active at shallower dips (e.g., Collettini, 2011) and may resolve the apparent mechanical paradox of these anomalously low-angle structures. Although prior experimental friction studies of LANF zone rocks show some evidence of friction coefficients of 0.2 – 0.3 in the most phyllosilicate-rich or heavily foliated samples, many previously tested gouges show friction coefficients >0.4 (Collettini et al., 2009b; Haines et al., 2014; Smith & Faulkner, 2010; Niemeijer & Collettini, 2014; Numelin et al., 2007b). Our results confirm that shallow LANF gouges can be extremely frictionally weak, but suggest that LANF strength at greater depths depends on the frictional strength of the deeper fault rock protoliths of these gouges.

4.1.2. Depth-dependent frictional stability

One explanation for the paucity of recorded earthquakes on some LANFs is that they primarily creep aseismically (e.g., Abers, 2009; Hreinsdóttir & Bennett, 2009), implying that the fault material is predominantly velocity-strengthening through the brittle crust (e.g., Collettini, 2011). Indeed, velocity-stepping experiments on exhumed LANF gouges (Niemeijer & Colletini, 2013; Numelin et al., 2007b; Smith & Faulkner, 2010) and typical LANF gouge minerals (Collettini, 2011 and references within) show predominantly velocity-strengthening behavior under upper crustal conditions, with a thermally activated transition to velocity-weakening behavior at >300 °C (Niemeijer & Collettini, 2014).

Velocity-stepping experiments on Mai'iu fault sequence rocks ranging from mylonitic protoliths to well-developed gouges were performed under a range of temperature (50 – 450 °C), effective normal stress (30 – 210 MPa), and pore-fluid pressure (20 – 140 MPa) conditions associated with a range of crustal depths (~3 – 25 km, as inferred by Mizera et al., 2019). The saponite-rich gouges exhibit strictly velocity-strengthening behavior for temperatures <150 °C, with the less-saponitic sample transitioning to velocity-weakening at T≥150 °C. In contrast, mild velocity-weakening behavior is observed for low upstep-velocities at T=50-200 °C in the mafic gouges, which contain less saponite (< 22%) and more remnant (ultra-)mafic clasts, chlorite, actinolite and epidote. The mafic gouges transition to velocity-strengthening with increasing upstep-velocity. These results suggest that the Mai'iu fault likely creeps at T<150 °C (<~6 km depth), but that local fault stability depends on the proportion of saponite to mafic components in the gouge. The hydrological and thermochemical conditions that promote the formation and accumulation of saponite appear crucial to development of frictionally weak, velocity-strengthening behavior in the upper reaches of the fault zone.

The fault rocks active at greater depths (>~6 km, based on temperatures >150 °C from Mizera et al., submitted) are more strongly and consistently velocity-weakening than any of the shallowly formed gouges. The cataclasites and ultracataclasite samples show predominantly negative *(a–b)* values (-0.02 < *(a–b)* < 0) at 150-350 °C, transitioning to consistently positive *(a-b)* values (0 < *(a–b)* < 0.05) at ≥400 °C. This transition to velocity-strengthening behavior around T=400 °C corresponds to the conditions under which most chlorite and chlorite-actinolite gouges have been observed to be strongly velocity-strengthening (T ≥ 400 °C and $\sigma_n^{eff} = P_f \geq$ 100 MPa, Okamoto et al., 2019, 2020). We infer that deformation at depths greater than the ~400 °C isotherm (> ~20-25 km depth) occurs primarily by aseismic ductile creep in the mafic mineral assemblage (chlorite, actinolite) within the mylonitic shear zone.

Altogether, the experimental friction results outline three primary temperature-dependent stability regimes of the Mai'iu fault rock sequence: low-temperature (≤ 150 °C) velocity-strengthening, intermediate-temperature (150-350 °C) velocity-weakening, and high-temperature velocity-strengthening (400-450 °C). Because the driving velocity in our experiments (1 μm/s) is orders of magnitude faster than natural tectonic plate rates, the frictional stability transitions observed in each rock type may shift to somewhat lower temperatures at slower deformation rates, as predicted by microphysical models (e.g., Chen et al., 2017 and references therein). In addition, laboratory experiments and geological mapping cannot constrain the size and spatial distribution of frictionally locked patches, which are determined by a variety of factors including the spatial distribution of different fault rocks and gouge minerals, local thermal structure, fault roughness and architectural complexity, presence and distribution of pore fluids, and local history and heterogeneity of stress and slip on the fault, among others (e.g., Avouac, 2015; Burgmann, 2018; Harris, 2017; Scholz, 2019; references within).

4.2. Contemporary slip behavior in the context of geological and experimental evidence

GPS velocities near the active Mai'iu LANF reveal ~8 mm/yr of horizontal extension corresponding to ~10 mm/yr dip-slip on a normal fault dipping 26-35°. Horizontal velocities are fit similarly well by ~10 mm/yr of dip-slip with distinctly different distributions of interseismic fault locking: 1) aseismic creep below a shallowly locked patch (~2 km deep) that projects to the surface at the main fault trace; or 2) aseismic creep updip and downdip of a deeper locked patch (locked from ~5-16 km depth) that projects to the surface along a splay fault within the hanging-wall. We evaluate these two scenarios with respect to the experimental friction results alongside geological and geophysical evidence of Mai'iu fault slip.

The strongly velocity-strengthening behavior of the shallowest saponitic Mai'iu fault gouges (Figure 7a) suggests frictionally stable creep near the surface, while the predominantly velocity-weakening behavior of the cataclastic fault units deformed at greater depths (Figures 7b,d) points to deeper seismic slip and interseismic locking. The largely velocity-weakening behavior of the cataclasites and ultracataclasites from T=150-350 °C implies that frictional fault slip from ~8-20 km depth likely occurs as seismic or microseismic events that release elastic strain accumulated around frictionally locked patches. Along with evidence for sufficient seismic slip to generate pseudotachylite melts at 10-12 km depth (Little et al., 2019) and cause episodic meter-scale coastal uplifts further along-strike (Biemiller et al., 2018), these results are most consistent with model 2 (Figure 3d-f), which exhibits strong locking over the ~5-16 km depth range and would predict both earthquake nucleation and relatively uninhibited earthquake propagation through frictionally unstable velocity-weakening fault rocks (Figures 6-8). Model 1, by contrast, predicts aseismic creep below 2 km depth and negligible seismogenic potential at the depths of pseudotachylite formation and velocity weakening fault rocks. Although seismic rupture nucleated elsewhere could potentially propagate through a creeping segment to generate pseudotachylites, the depth-dependent stratification of fault slip stability illustrated by experimental friction and microstructural evidence implies deeper, stronger locking most consistent with model 2.

Frequent and localized microseismicity is common along actively creeping fault segments (e.g., Burgmann et al., 2000; Harris, 2017; Malservisi et al., 2005; Wolfson-Schwehr & Boettcher, 2019). Strongly aligned microseismicity from 12-25 km depth not only outlines the deeper extent of the Mai'iu fault, but also suggests that this portion of the fault zone actively creeps, generating microseismic events during frictional failure of small locked asperities within the creeping shear zone. The updip cutoff depth of this microseismicity around 12 km suggests a transition from steady creep below to stronger locking above, and may be associated with a transition from frictional-viscous velocity-strengthening creep to frictional velocity-weakening behavior around 10-15 km (Figure 8). Such depth-dependent mechanical transitions may be explained by our experimentally observed frictional transition from velocity-weakening to velocity-strengthening behavior in the cataclastic fault rocks at around 400 °C (Figures 6-7), as well as the microstructurally recorded mixed frictional-viscous deformation in the cataclasites and mylonites (Little et al., 2019; Mizera et al., submitted). The general depth range of this mechanical transition agrees well with model 2's predicted coupling transition from stronger locking around 5-16 km depth to creep downdip of this region; this coupling transition is not predicted by model 1 (Figures 3, 8). Combining our geodetic results with the diverse geological, experimental and seismological evidence for mixed seismic slip and aseismic creep, we infer that the Mai'iu fault is more strongly locked and potentially seismogenic from ~5-16 km depth and creeps both updip and downdip of this zone (model 2; Figure 8).

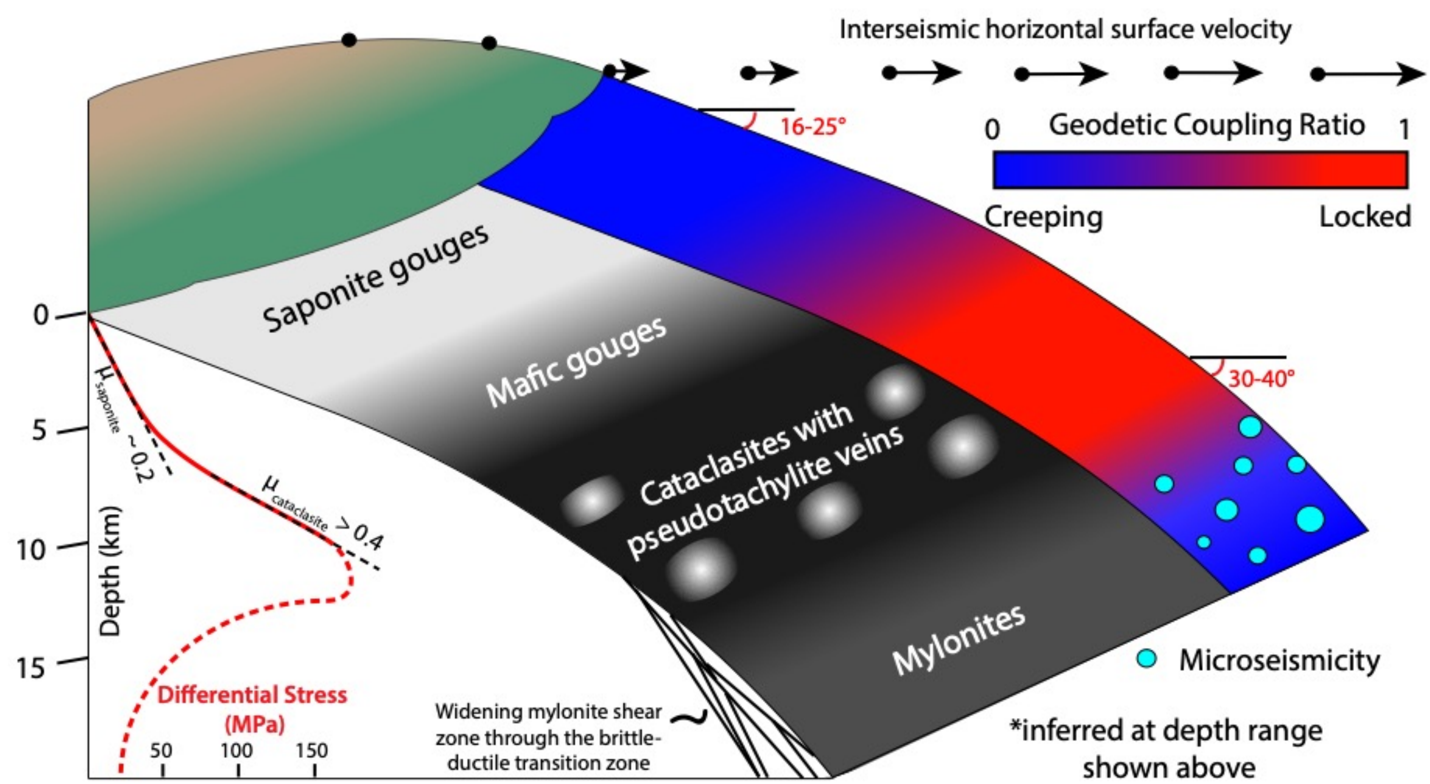

Fault Rock Unit	Friction Coefficient	Frictional Stability*	Deformation Mechanism*
Saponite gouges	0.11 - 0.28	Velocity-strengthening	Aseismic frictional creep
Mafic gouges	0.22 - 0.57	Velocity-weakening to velocity-strengthening	Mixed diffusion creep, frictional-viscous creep & seismic slip ('partial locking')
Cataclasites with pseudotachylite veins	0.44 - 0.80	Both velocity-weakening and velocity-strengthening	
Mylonites	0.6 - 0.8	Both velocity-weakening and velocity-strengthening	Diffusion creep, grain-boundary sliding, small frictional failures

Figure 8. Inferred distribution of active Mai'iu fault rocks and deformation mechanisms, along with the resulting geodetic coupling and horizontal surface velocities. Stronger locking occurs in the velocity-weakening cataclastic units, while stable interseismic creep occurs updip and downdip of this zone in the saponite gouges and mylonites, respectively. Frictional stability and strength derived from experiments (Figures 6-7) for all units except the mylonites, for which frictional behavior is inferred from microstructures (Little et al., 2019; Mizera et al., submitted) and microseismicity (Abers, 2016). The differential stress profile is based on frictional strength above the brittle-ductile transition zone (solid line) and is inferred only schematically below (dashed line).

4.3 Mechanical implications for LANFs

Active aseismic LANF creep below a shallow locking depth (model 1) would agree well with previous geodetic inferences of shallow aseismic creep on another active LANF, the Altotiberina fault (Hreinsdóttir & Bennett, 2009). However, allowing for more complex structures including creep and locking of nearby splay faults, subsequent modeling of the Altotiberina fault (Anderlini et al., 2016) has shown that a spatially heterogeneous pattern of locked and creeping patches is more consistent with observed surface GPS velocities. Similarly, based on the velocity-weakening frictional behavior of exhumed fault rocks, coseismically generated pseudotachylites exhumed from ~10–12 km depth, microseismicity data highlighting fault creep below ~12 km depth, and the results of geodetic models that allow for splay fault slip and patchy locking at depth, the Mai'iu fault appears to be more strongly locked from ~5–16 km depth (model 2) and to be creeping interseismically along its shallowest portions (<~5 km depth).

We suggest that the strongly coupled depth range of ~5-16 km corresponds to the brittle strength peak for the Mai'iu fault rock sequence where interseismic elastic strain can accumulate between periods of cataclastic deformation of potentially unstable velocity-weakening mylonitic protoliths (i.e., cataclasite and ultracataclasite units, Figures 5-7). With progressive slip and exhumation, fluid-assisted chemical reactions precipitate frictionally stable velocity-strengthening phyllosilicate gouge minerals (clays such as saponite; Figure 7a), responsible for the apparent transition towards aseismic creep near the surface. Models with deep locking below ~15 km do not fit the GPS data well (Figures 4, S4, S6); therefore, we infer that downdip of the strongly locked portion, slip occurs mostly by aseismic diffusive mass transfer creep processes, punctuated by microseismicity associated with occasional failure of small locked asperities and the fracturing of intact competent clasts within the primarily ductilely-deforming shear zone and also by the infrequent downdip propagation of large earthquake slip.

This interpretation of slip on the Mai'iu fault implies that it may be capable of hosting and even nucleating sizeable, albeit relatively infrequent, earthquakes. Assuming a typical dip-slip rupture width-length ratio of 0.668 (Leonard, 2010) and shear modulus of 25 GPa, nominal slip of 1 m on a locked patch dipping 35° from 5-16 km depth would correspond to a ~M_w 6.7 earthquake; allowing for rupture to the surface increases this estimate to ~M_w 7.0. These estimated magnitudes agree well with both the largest reported LANF earthquake globally (M_w 6.8, 29 October 1985; Abers, 2001; Abers et al., 1997) and estimations of Mai'iu fault earthquake magnitude based on the stress and slip required for coseismic melting and pseudotachylite formation (M_w 6.0+; Little et al., 2019). Taken together, these observations and calculations illustrate the potential severity of Mai'iu fault earthquakes and the importance of including the Mai'iu fault and other active LANFs in future seismic hazard assessments and risk mitigation plans.

5.0 Conclusions

New campaign GPS and experimental friction data from the Mai'iu fault in Papua New Guinea illuminate the patterns and mechanisms of creep and locking on one of the world's fastest-slipping, active low-angle normal faults. Horizontal GPS velocities indicate 8.3±1.2 mm/yr of active extension across the Mai'iu fault. Friction experiments show that clay-rich gouges from the shallowest and most poorly aligned portion of the fault are both weak (μ = 0.11-0.35) and predominantly velocity-strengthening, while cataclastic fault rocks deformed at greater depths on more steeply dipping parts of the fault are stronger (μ = 0.44-0.84) and predominantly velocity-weakening. Two distinct fault locking models fit the GPS data equally well: one that requires aseismic creep below ~2 km depth and one with a locked patch from ~5-16 km depth. A range of geological, experimental, and seismological data support the geodetic model with interseismic locking from ~5-16 km depth and shallower aseismic creep on the Mai'iu fault and one or more hanging wall splay faults. This model also agrees with geological and coral paleoseismological evidence of seismic slip on the Mai'iu fault and confirms that LANFs may be capable of hosting M_w 7.0+ earthquakes despite the abundance of velocity-strengthening fault gouges at shallow depths which promote interseismic creep near the Earth's surface.

Acknowledgments & Data Availability

We first and foremost thank the people of Milne Bay and Oro provinces in Papua New Guinea for their support and hospitality, without which the field-based components would not have been possible. We thank Samuel Webber, Neville Palmer, and Rory Hart for field and technical support. We thank Samuel Webber, Jürgen Österle, Daniel Stockli, Kevin Norton, and Whitney Behr for helpful discussions. This study was supported by the US National Science Foundation grant EAR-1524729 (L.W., L.L, J.B.) and graduate student fellowship program (J.B.), New Zealand Royal Society Marsden Fund grant VUW1310 (T.L., C.B., M.M., S.E.), European Research Council grant SEISMIC (335915) (A.N.), and the Dutch Research Council VIDI grant 854.12.011 (A.N.).

Experimental friction data and GPS velocities are given in the Supporting Information. GPS data are available through the UNAVCO data portal <link and DOI to be added> Experimental friction data are available through the YODA online repository of the Utrecht University (https://geo.yoda.uu.nl), as <link and DOI to be added>.

Abers, G. A., Eilon, Z., Gaherty, J. B., Jin, G., Kim, Y., Obrebski, M., & Dieck, C. (2016). Southeast Papuan crustal tectonics: Imaging extension and buoyancy of an active rift. *Journal of Geophysical Research: Solid Earth*, *121*(2), 951–971. https://doi.org/10.1002/2015JB012621

Abers, G. a. (2001). Evidence for seismogenic normal faults at shallow dips in continental rifts. *Geological Society, London, Special Publications*, *187*(1), 305–318. https://doi.org/10.1144/GSL.SP.2001.187.01.15

Abers, G. A. (2009). Slip on shallow-dipping normal faults. *Geology*, *37*(8), 767–768. https://doi.org/10.1130/focus082009.1.

Abers, G. A. (1991). Possible seismogenic shallow-dipping normal faults in the Woodlark-D'Entrecasteaux extensional province, Papua New Guinea. *Geology*, *19*(12), 1205–1208. https://doi.org/10.1130/0091-7613(1991)019<1205:pssdnf>2.3.co;2

Abers, G. A., Mutter, C. Z., & Fang, J. (1997). Shallow dips of normal faults during rapid extension: Earthquakes in the Woodlark-D'Entrecasteaux rift system, Papua New Guinea. *Journal of Geophysical Research: Solid Earth*, *102*(B7), 15301–15317. https://doi.org/10.1029/97jb00787

Almeida, R., Lindsey, E. O., Bradley, K., Hubbard, J., Mallick, R., & Hill, E. M. (2018). Can the Updip Limit of Frictional Locking on Megathrusts Be Detected Geodetically? Quantifying the Effect of Stress Shadows on Near-Trench Coupling. *Geophysical Research Letters*, *45*(10), 4754–4763. https://doi.org/10.1029/2018GL077785

Anderlini, L., Serpelloni, E., & Belardinelli, M. E. (2016). Creep and locking of a low-angle normal fault: Insights from the Altotiberina fault in the Northern Apennines (Italy). *Geophysical Research Letters*, *43*(9), 4321–4329. https://doi.org/10.1002/2016GL068604

Anzidei, M., Boschi, E., Cannelli, V., Devoti, R., Esposito, A., Galvani, A., … Serpelloni, E. (2009). Coseismic deformation of the destructive April 6, 2009 L'Aquila earthquake (central Italy) from GPS data. *Geophysical Research Letters*, *36*(17). https://doi.org/10.1029/2009GL039145

Araki, E., Saffer, D. M., Kopf, A. J., Wallace, L. M., Kimura, T., Machida, Y., … Davis, E. (2017). Recurring and triggered slow-slip events near the trench at the Nankai Trough subduction megathrust. *Science*, *356*(6343), 1157–1160. https://doi.org/10.1126/science.aan3120

Avouac, J.-P. (2015). From Geodetic Imaging of Seismic and Aseismic Fault Slip to Dynamic Modeling of the Seismic Cycle. *Annual Review of Earth and Planetary Sciences*, *43*(1), 233–271. https://doi.org/10.1146/annurev-earth-060614-105302

Axen, G. J. (1992). Pore pressure, stress incraese, and fault weakening in low-angle normal faulting. *Journal of Geophysical Research*, *97*(B6), 8979–8991.

Axen, G. J. (2004). Mechanics of Low-Angle Normal Faults. In *Rheology and Deformation of the Lithosphere at Continental Margins*. Columbia University Press. https://doi.org/10.7312/karn12738-004

Baldwin, S. L., Fitzgerald, P. G., & Webb, L. E. (2012). Tectonics of the New Guinea Region. *Annual Review of Earth and Planetary Sciences*, *40*(1), 495–520. https://doi.org/10.1146/annurev-earth-040809-152540

Banerjee, P., Pollitz, F. F., & Bürgmann, R. (2005). The Size and Duration of the Sumatra-Andaman Earthquake from Far-Field Static Offsets. *Science*, *308*(5729).

Beavan, J., Denys, P., Denham, M., Hager, B., Herring, T., & Molnar, P. (2010). Distribution of present-day vertical deformation across the Southern Alps, New Zealand, from 10 years of GPS data. *Geophysical Research Letters*, *37*(16), n/a-n/a. https://doi.org/10.1029/2010GL044165

Beavan, J., Moore, M., Pearson, C., Henderson, M., Parsons, B., Bourne, S., … Hodgkinson, K. (1999). Crustal deformation during 1994-1998 due to oblique continental collision in the central Southern Alps, New Zealand, and implications for seismic potential of the Alpine fault. *Journal of Geophysical Research: Solid Earth*, *104*(B11), 25233–25255. https://doi.org/10.1029/1999jb900198

Behnsen, J., & Faulkner, D. R. (2012). The effect of mineralogy and effective normal stress on frictional strength of sheet silicates. *Journal of Structural Geology*, *42*, 49–61. https://doi.org/10.1016/j.jsg.2012.06.015

Bennett, R. A., Hreinsdóttir, S., Velasco, M. S., & Fay, N. P. (2007). GPS constraints on vertical crustal motion in the northern Basin and Range. *Geophysical Research Letters*, *34*(22), L22319. https://doi.org/10.1029/2007GL031515

Biemiller, J., Wallace, L. M., Ellis, S. M., Little, T. A., Lavier, L., Mizera, M., … Webber, S. M. (2018). Short- and Long-term Deformation Styles on an Active Low-angle Normal Fault: Mai'iu Fault, Papua New Guinea. *AGUFM*, *2018*, T33D-0430.

Boulton, C., Barth, N. C., Moore, D. E., Lockner, D. A., Townend, J., & Faulkner, D. R. (2018). Frictional properties and 3-D stress analysis of the southern Alpine Fault, New Zealand. *Journal of Structural Geology*, *114*, 43–54. https://doi.org/10.1016/j.jsg.2018.06.003

Burgmann, R., Schmidt, D., Nadeau, R. M., d'Alessio, M., Fielding, E., Manaker, D., … Murray, M. H. (2000). Earthquake potential along the Northern Hayward fault, California. *Science*, *289*(5482), 1178–1182. https://doi.org/10.1126/science.289.5482.1178

Bürgmann, R. (2018). The geophysics, geology and mechanics of slow fault slip. *Earth and Planetary Science Letters*, *495*, 112–134. https://doi.org/10.1016/j.epsl.2018.04.062

Chen, J., Niemeijer, A. R., & Spiers, C. J. (2017). Microphysically Derived Expressions for Rate-and-State Friction Parameters, a, b, and Dc. *Journal of Geophysical Research: Solid Earth*, *122*(12), 9627–9657. https://doi.org/10.1002/2017JB014226

Chester, F. M., & Higgs, N. G. (1992). Multimechanism friction constitutive model for ultrafine quartz gouge at hypocentral conditions. *Journal of Geophysical Research: Solid Earth*, *97*(B2), 1859–1870. https://doi.org/10.1029/91JB02349

Chiaraluce, L., Chiarabba, C., Collettini, C., Piccinini, D., & Cocco, M. (2007). Architecture and mechanics of an active low-angle normal fault: Alto Tiberina Fault, northern Apennines, Italy. *Journal of Geophysical Research*, *112*(B10), B10310. https://doi.org/10.1029/2007JB005015

Chiaraluce, L., Amato, A., Carannante, S., Castelli, V., Cattaneo, M., Cocco, M., … Valoroso, L. (2014). The alto Tiberina near fault observatory (northern Apennines, Italy). *Annals of Geophysics*, *57*(3). https://doi.org/10.4401/ag-6426

Choi, E., & Buck, W. R. (2012). Constraints on the strength of faults from the geometry of rider blocks in continental and oceanic core complexes. *Journal of Geophysical Research: Solid Earth*, *117*(B4), n/a-n/a. https://doi.org/10.1029/2011JB008741

Choi, E., Buck, W. R., Lavier, L. L., & Petersen, K. D. (2013). Using core complex geometry to constrain fault strength. *Geophysical Research Letters*, *40*(15), 3863–3867. https://doi.org/10.1002/grl.50732

Collettini, C., & Barchi, M. R. (2004). A comparison of structural data and seismic images for low-angle normal faults in the Northern Apennines (Central Italy): Constraints on activity. *Geological Society Special Publication*, *224*, 95–112. https://doi.org/10.1144/GSL.SP.2004.224.01.07

Collettini, C., Tesei, T., Scuderi, M. M., Carpenter, B. M., & Viti, C. (2019). Beyond Byerlee friction, weak faults and implications for slip behavior. *Earth and Planetary Science Letters*, *519*, 245–263. https://doi.org/10.1016/j.epsl.2019.05.011

Collettini, C. (2011). The mechanical paradox of low-angle normal faults: Current understanding and open questions. *Tectonophysics*, *510*(3–4), 253–268. https://doi.org/10.1016/j.tecto.2011.07.015

Collettini, C., Niemeijer, A., Viti, C., & Marone, C. (2009b). Fault zone fabric and fault weakness. *Nature*, *462*(7275), 907–910. https://doi.org/10.1038/nature08585

Collettini, C., & Sibson, R. H. (2001). Normal faults, normal friction? *Geology*, *29*(10), 927. https://doi.org/10.1130/0091-7613(2001)029<0927:NFNF>2.0.CO;2

Collettini, C., Viti, C., Smith, S. A. F., & Holdsworth, R. E. (2009a). Development of interconnected talc networks and weakening of continental low-angle normal faults. *Geology*, *37*(6), 567–570. https://doi.org/10.1130/G25645A.1

Daczko, N. R., Caffi, P., Halpin, J. A., & Mann, P. (2009). Exhumation of the Dayman dome metamorphic core complex, eastern Papua New Guinea. *Journal of Metamorphic Geology*, *27*(6), 405–422. https://doi.org/10.1111/j.1525-1314.2009.00825.x

Dieterich, J. H. (1979). Modeling of rock friction: 1. Experimental results and constitutive equations. *Journal of Geophysical Research*, *84*(B5), 2161. https://doi.org/10.1029/JB084iB05p02161

Dieterich, J. H. (2013). Constitutive Properties of Faults With Simulated Gouge (pp. 103–120). American Geophysical Union (AGU). https://doi.org/10.1029/gm024p0103

Duba, A. G., Durham, W. B., Handin, J. W., & Wang, H. F. (Eds.). (1990). *The Brittle-Ductile Transition in Rocks* (Vol. 56). Washington, D. C.: American Geophysical Union. https://doi.org/10.1029/GM056

Dziewonski, A. M., & Anderson, D. L. (1981). *Preliminary reference Earth model* *. *Preliminary reference Earth modeL Phys. Earth Planet. Inter* (Vol. 25).

Floyd, J. S., Mutter, J. C., Goodliffe, A. M., & Taylor, B. (2001). Evidence for fault weakness and fluid flow within an active low-angle normal fault. *Nature*, *411*(6839), 779–783. https://doi.org/10.1038/35081040

Gu, J. C., Rice, J. R., Ruina, A. L., & Tse, S. T. (1984). Slip motion and stability of a single degree of freedom elastic system with rate and state dependent friction. *Journal of the Mechanics and Physics of Solids*, *32*(3), 167–196. https://doi.org/10.1016/0022-5096(84)90007-3

Haines, S., Marone, C., & Saffer, D. (2014). Frictional properties of low-angle normal fault gouges and implications for low-angle normal fault slip. *Earth and Planetary Science Letters*, *408*, 57–65. https://doi.org/10.1016/j.epsl.2014.09.034

Harris, R. A. (2017, March 1). Large earthquakes and creeping faults. *Reviews of Geophysics*. Blackwell Publishing Ltd. https://doi.org/10.1002/2016RG000539

Hayes, G. P. (2017). The finite, kinematic rupture properties of great-sized earthquakes since 1990. *Earth and Planetary Science Letters*, *468*, 94–100. https://doi.org/10.1016/j.epsl.2017.04.003

He, C., Luo, L., Hao, Q.-M., & Zhou, Y. (2013). Velocity-weakening behavior of plagioclase and pyroxene gouges and stabilizing effect of small amounts of quartz under hydrothermal conditions. *Journal of Geophysical Research: Solid Earth*, *118*(7), 3408–3430. https://doi.org/10.1002/jgrb.50280

Herring, T. A., Floyd, M. A., King, R. W., & McClusky, S. C. (2015). GLOBK Reference Manual. Masschusetts Institute of Technology.

Herring, T. A., King, R. W.Floyd, M. A., & McClusky, S. C. (2018). GAMIT Reference Manual. Masschusetts Institute of Technology.

Hreinsdóttir, S., & Bennett, R. A. (2009). Active aseismic creep on the Alto Tiberina low-angle normal fault, Italy. *Geology*, *37*(8), 683–686. https://doi.org/10.1130/G30194A.1

Ikari, M. J., & Kopf, A. J. (2017). Seismic potential of weak, near-surface faults revealed at plate tectonic slip rates. *Science Advances*, *3*(11), e1701269. https://doi.org/10.1126/sciadv.1701269

Ikari, M. J., Marone, C., & Saffer, D. M. (2011). On the relation between fault strength and frictional stability. *Geology*, *39*(1), 83–86. https://doi.org/10.1130/G31416.1

Ikari, M. J., Saffer, D. M., & Marone, C. (2009). Frictional and hydrologic properties of clay-rich fault gouge. *Journal of Geophysical Research: Solid Earth*, *114*(5). https://doi.org/10.1029/2008JB006089

Jackson, J. A. (1987). Active normal faulting and crustal extension. *Geological Society Special Publication*, *28*, 3–17. https://doi.org/10.1144/GSL.SP.1987.028.01.02

Jackson, J. A., & White, N. J. (1989). Normal faulting in the upper continental crust: observations from regions of active extension. *Journal of Structural Geology*, *11*(1–2), 15–36. https://doi.org/10.1016/0191-8141(89)90033-3

Jackson, J., & McKenzie, D. (1983). The geometrical evolution of normal fault systems. *Journal of Structural Geology*, *5*(5), 471–482. https://doi.org/10.1016/0191-8141(83)90053-6

Koulali, A., Tregoning, P., McClusky, S., Stanaway, R., Wallace, L., & Lister, G. (2015). New Insights into the present-day kinematics of the central and western Papua New Guinea from GPS. *Geophysical Journal International*, *202*(2), 993–1004. https://doi.org/10.1093/gji/ggv200

Lavier, L. L., Buck, W. R., & Poliakov, A. (1999). Self-consistent rolling-hinge model for the evolution of large-onset low-angle normal faults. *Geology*, *27*(12), 1127–1130. https://doi.org/10.1130/0091-7613(1999)027<1127:SCRHMF>2.3.CO;2

Lavier, L. L., Buck, W. R., & Poliakov, A. N. B. (2000). Factors controlling normal fault offset in an ideal brittle layer. *Journal of Geophysical Research: Solid Earth*, *105*(B10), 23431–23442. https://doi.org/10.1029/2000JB900108

Lay, T., Ye, L., Ammon, C. J., & Kanamori, H. (2017). Intraslab rupture triggering megathrust rupture coseismically in the 17 December 2016 Solomon Islands M_w 7.9 earthquake. *Geophysical Research Letters*, *44*(3), 1286–1292. https://doi.org/10.1002/2017GL072539

Lee, S., Lin, T., Feng, K., & Liu, T. (2018). Composite Megathrust Rupture From Deep Interplate to Trench of the 2016 Solomon Islands Earthquake. *Geophysical Research Letters*, *45*(2), 674–681. https://doi.org/10.1002/2017GL076347

Leonard, M. (2010). Earthquake fault scaling: Self-consistent relating of rupture length, width, average displacement, and moment release. *Bulletin of the Seismological Society of America*, *100*(5 A), 1971–1988. https://doi.org/10.1785/0120090189

Little, T. A., Hacker, B. R., Gordon, S. M., Baldwin, S. L., Fitzgerald, P. G., Ellis, S., & Korchinski, M. (2011). Diapiric exhumation of Earth's youngest (UHP) eclogites in the gneiss domes of the D'Entrecasteaux Islands, Papua New Guinea. *Tectonophysics*, *510*(1–2), 39–68. https://doi.org/10.1016/j.tecto.2011.06.006

Little, T. A., Baldwin, S. L., Fitzgerald, P. G., & Monteleone, B. (2007). Continental rifting and metamorphic core complex formation ahead of the Woodlark spreading ridge, D'Entrecasteaux Islands, Papua New Guinea. *Tectonics*, *26*(1), 1–26. https://doi.org/10.1029/2005TC001911

Little, T. A., Webber, S. M., Mizera, M., Boulton, C., Oesterle, J., Ellis, S., … Wallace, L. (2019). Evolution of a rapidly slipping, active low-angle normal fault, Suckling-Dayman metamorphic core complex, SE Papua New Guinea. *GSA Bulletin*. https://doi.org/10.1130/B35051.1

Lockner, D. A., Morrow, C., Moore, D., & Hickman, S. (2011). Low strength of deep San Andreas fault gouge from SAFOD core. *Nature*, *472*(7341), 82–86. https://doi.org/10.1038/nature09927

Malservisi, R., Furlong, K. P., & Gans, C. R. (2005). Microseismicity and creeping faults: Hints from modeling the Hayward fault, California (USA). *Earth and Planetary Science Letters*, *234*(3–4), 421–435. https://doi.org/10.1016/j.epsl.2005.02.039

Mann, P., Horton, B. K., Taylor, F. W., Shen, C., Lin, K., Renema, W., … Renema, W. (2009). Uplift patterns of reef terraces and sedimentary rocks constrain tectonic models for metamorphic core complexes in eastern Papua New Guinea. *AGUFM*, *2009*, G33B-0642.

Mann, P., & Taylor, F. W. (2002). Emergent Late Quaternary Coral Reefs of Eastern Papua New Guinea Constrain the Regional Pattern of Oceanic Ridge Propagation. *AGUFM*, *2002*, T52C-1206.

Marone, C. (1998). LABORATORY-DERIVED FRICTION LAWS AND THEIR APPLICATION TO SEISMIC FAULTING. *Annual Review of Earth and Planetary Sciences*, *26*(1), 643–696. https://doi.org/10.1146/annurev.earth.26.1.643

Mccaffrey, R. (2013). Crustal Block Rotations and Plate Coupling (pp. 101–122). American Geophysical Union (AGU). https://doi.org/10.1029/gd030p0101

Mizera, M., Little, T. A., Biemiller, J., Ellis, S., Webber, S., & Norton, K. P. (2019). Structural and Geomorphic Evidence for Rolling-Hinge Style Deformation of an Active Continental Low-Angle Normal Fault, SE Papua New Guinea. *Tectonics*, *38*(5), 1556–1583. https://doi.org/10.1029/2018TC005167

Moore, D. E. (2014). Comparative mineral chemistry and textures of SAFOD fault gouge and damage-zone rocks. *Journal of Structural Geology*, *68*(PA), 82–96. https://doi.org/10.1016/j.jsg.2014.09.002

Niemeijer, A. R., Boulton, C., Toy, V. G., Townend, J., & Sutherland, R. (2016). Large-displacement, hydrothermal frictional properties of DFDP-1 fault rocks, Alpine Fault, New Zealand: Implications for deep rupture propagation. *Journal of Geophysical Research: Solid Earth*, *121*(2), 624–647. https://doi.org/10.1002/2015JB012593

Niemeijer, A. R., Boulton, C., Toy, V. G., Townend, J., & Sutherland, R. (2016). Large-displacement, hydrothermal frictional properties of DFDP-1 fault rocks, Alpine Fault, New Zealand: Implications for deep rupture propagation. *Journal of Geophysical Research: Solid Earth*, *121*(2), 624–647. https://doi.org/10.1002/2015JB012593

Niemeijer, A. R., & Collettini, C. (2014). Frictional Properties of a Low-Angle Normal Fault Under In Situ Conditions: Thermally-Activated Velocity Weakening. *Pure and Applied Geophysics*, *171*(10), 2641–2664. https://doi.org/10.1007/s00024-013-0759-6

Numelin, T., Marone, C., & Kirby, E. (2007b). Frictional properties of natural fault gouge from a low-angle normal fault, Panamint Valley, California. *Tectonics*, *26*(2), n/a-n/a. https://doi.org/10.1029/2005TC001916

Numelin, T., Kirby, E., Walker, J. D., & Didericksen, B. (2007a). Late Pleistocene slip on a low-angle normal fault, Searles Valley, California. *Geosphere*, *3*(3), 163–176. https://doi.org/10.1130/GES00052.1

Okada, Y. (1985). Surface deformation due to shear and tensile faults in a half-space. *Bulletin of the Seismological Society of America*, *75*(4), 1135–1154.

Okamoto, A. S., Niemeijer, A. R., Takeshita, T., Verberne, B. A., & Spiers, C. J. (2020). Frictional properties of actinolite-chlorite gouge at hydrothermal conditions. *Tectonophysics*, *779*, 228377. https://doi.org/10.1016/j.tecto.2020.228377

Okamoto, A. S., Verberne, B. A., Niemeijer, A. R., Takahashi, M., Shimizu, I., Ueda, T., & Spiers, C. J. (2019). Frictional Properties of Simulated Chlorite Gouge at Hydrothermal Conditions: Implications for Subduction Megathrusts. *Journal of Geophysical Research: Solid Earth*, *124*(5), 4545–4565. https://doi.org/10.1029/2018JB017205

Österle, J. E., Little, T. A., Seward, D., Stockli, D. F., & Gamble, J. (2020). The petrology, geochronology and tectono-magmatic setting of igneous rocks in the Suckling-Dayman metamorphic core complex, Papua New Guinea. *Gondwana Research*. https://doi.org/10.1016/j.gr.2020.01.014

Platt, J. P., Behr, W. M., & Cooper, F. J. (2015). Metamorphic core complexes: windows into the mechanics and rheology of the crust. *Journal of the Geological Society*, *172*(1), 9–27. https://doi.org/10.1144/jgs2014-036

Pollitz, F. F. (1996). Coseismic Deformation From Earthquake Faulting On A Layered Spherical Earth. *Geophysical Journal International*, *125*(1), 1–14. https://doi.org/10.1111/j.1365-246X.1996.tb06530.x

Reinen, L. A., & Weeks, J. D. (1993). Determination of rock friction constitutive parameters using an iterative least squares inversion method. *Journal of Geophysical Research*, *98*(B9), 15937–15950. https://doi.org/10.1029/93jb00780

Rice, J. R., & Tse, S. T. (1986). Dynamic motion of a single degree of freedom system following a rate and state dependent friction law. *Journal of Geophysical Research*, *91*(B1), 521. https://doi.org/10.1029/JB091iB01p00521

Ross, J. V., & Lewis, P. D. (1989). Brittle-ductile transition: semi-brittle behavior. *Tectonophysics*, *167*(1), 75–79. https://doi.org/10.1016/0040-1951(89)90295-3

Ruina, A. (1983). Slip instability and state variable friction laws. *Journal of Geophysical Research: Solid Earth*, *88*(B12), 10359–10370. https://doi.org/10.1029/JB088iB12p10359

Ruppel, C. (1995). Extensional processes in continental lithosphere. *Journal of Geophysical Research*, *100*(B12). https://doi.org/10.1029/95jb02955

Scholz, C. H. (2019). *The Mechanics of Earthquakes and Faulting* (3rd ed.). Cambridge: Cambridge University Press. https://doi.org/DOI: 10.1017/9781316681473

Serpelloni, E., Faccenna, C., Spada, G., Dong, D., & Williams, S. D. P. (2013). Vertical GPS ground motion rates in the Euro-Mediterranean region: New evidence of velocity gradients at different spatial scales along the Nubia-Eurasia plate boundary. *Journal of Geophysical Research: Solid Earth*, *118*(11), 6003–6024. https://doi.org/10.1002/2013JB010102

Smith, I. E., & Davies, H. L. (1976). *Geology of the Southeast Papuan Mainland*. Canberra: Australian Government Publishing Service for the Bureau of Mineral Resources, Geology and Geophysics.

Smith, S. A. F., & Faulkner, D. R. (2010). Laboratory measurements of the frictional properties of the Zuccale low-angle normal fault, Elba Island, Italy. *Journal of Geophysical Research: Solid Earth*, *115*(2). https://doi.org/10.1029/2008JB006274

Sone, H., Shimamoto, T., & Moore, D. E. (2012). Frictional properties of saponite-rich gouge from a serpentinite-bearing fault zone along the Gokasho-Arashima Tectonic Line, central

Japan. *Journal of Structural Geology*, *38*, 172–182. https://doi.org/10.1016/j.jsg.2011.09.007

Strasser, F. O., Arango, M. C., & Bommer, J. J. (2010). Scaling of the source dimensions of interface and intraslab subduction-zone earthquakes with moment magnitude. *Seismological Research Letters*, *81*(6), 941–950. https://doi.org/10.1785/gssrl.81.6.941

Taylor, B., Goodliffe, A. M., & Martinez, F. (1999). How continents break up: Insights from Papua New Guinea. *Journal of Geophysical Research: Solid Earth*, *104*(B4), 7497–7512. https://doi.org/10.1029/1998jb900115

Taylor, F. W., Briggs, R. W., Frohlich, C., Brown, A., Hornbach, M., Papabatu, A. K., … Billy, D. (2008). Rupture across arc segment and plate boundaries in the 1 April 2007 Solomons earthquake. *Nature Geoscience*, *1*(4), 253–257. https://doi.org/10.1038/ngeo159

Tregoning, P., Burgette, R., McClusky, S. C., Lejeune, S., Watson, C. S., & McQueen, H. (2013). A decade of horizontal deformation from great earthquakes. *Journal of Geophysical Research: Solid Earth*, *118*(5), 2371–2381. https://doi.org/10.1002/jgrb.50154

Tullis, J., & Yund, R. A. (1987). Transition from cataclastic flow to dislocation creep of feldspar. *Geology*, *15*(001), 606–609. https://doi.org/10.1130/0091-7613(1987)15<606:TFCFTD>2.0.CO

U.S. Geological Survey. (2019). Earthquake Hazards Program.

Valoroso, L., Chiaraluce, L., Di Stefano, R., & Monachesi, G. (2017). Mixed-Mode Slip Behavior of the Altotiberina Low-Angle Normal Fault System (Northern Apennines, Italy) through High-Resolution Earthquake Locations and Repeating Events. *Journal of Geophysical Research: Solid Earth*, *122*(12), 10,220-10,240. https://doi.org/10.1002/2017JB014607

Wallace, L. M., Taylor, F. W., Bevis, M. G., Phillips, D. A., Walter, J. I., Kendrick, E. C., … Papabatu, A. K. (2015). Interseismic, coseismic, postseismic, and slow slip event deformation above a shallow subduction thrust in the western Solomon Islands. *AGUFM*, *2015*, T44B-07.

Wallace, L. M., Ellis, S., Little, T., Tregoning, P., Palmer, N., Rosa, R., … Kwazi, J. (2014). Continental breakup and UHP rock exhumation in action: GPS results from the Woodlark Rift, Papua New Guinea. *Geochemistry, Geophysics, Geosystems*, *15*(11), 4267–4290. https://doi.org/10.1002/2014GC005458

Warren, J. M., & Hirth, G. (2006). Grain size sensitive deformation mechanisms in naturally deformed peridotites. *Earth and Planetary Science Letters*, *248*(1–2), 438–450. https://doi.org/10.1016/j.epsl.2006.06.006

Webber, S., Little, T. A., Norton, K. P., Österle, J., Mizera, M., Seward, D., & Holden, G. (2020). Progressive back-warping of a rider block atop an actively exhuming, continental low-angle normal fault. *Journal of Structural Geology*, *130*, 103906. https://doi.org/10.1016/j.jsg.2019.103906

Webber, S., Norton, K. P., Little, T. A., Wallace, L. M., & Ellis, S. (2018). How fast can low-angle normal faults slip? Insights from cosmogenic exposure dating of the active Mai'iu fault, Papua New Guinea. *Geology*, *46*(3), 227–230. https://doi.org/10.1130/G39736.1

Wernicke, B. (1995). Low-angle normal faults and seismicity: A review. *Journal of Geophysical Research: Solid Earth*, *100*(B10), 20159–20174. https://doi.org/10.1029/95JB01911

Williams, S. D. P., Bock, Y., Fang, P., Jamason, P., Nikoladi, R., Prawirodirdjo, L., … Johnson, D. (2004). Error analysis of continuous GPS position time series. *Journal of Geophysical Research*, *109*(B3). https://doi.org/10.1029/2003jb002741

Wolfson-Schwehr, M., & Boettcher, M. S. (2019). Global Characteristics of Oceanic Transform Fault Structure and Seismicity. In *Transform Plate Boundaries and Fracture Zones* (pp. 21–59). Elsevier. https://doi.org/10.1016/b978-0-12-812064-4.00002-5

Zhang, J., Bock, Y., Johnson, H., Fang, P., Williams, S., Genrich, J., … Behr, J. (1997). Southern California permanent GPS geodetic array: Error analysis of daily position estimates and site velocities. *Journal of Geophysical Research: Solid Earth*, *102*(B8), 18035–18055. https://doi.org/10.1029/97jb01380

Journal of Geophysical Research: Solid Earth

Supporting Information for

Mechanical implications of creep and partial coupling on the world's fastest slipping low-angle normal fault in southeastern Papua New Guinea

James Biemiller[1], Carolyn Boulton[2], Laura Wallace[1,3], Susan Ellis[3], Timothy Little[2], Marcel Mizera[2,4], Andre Niemeijer[4], Luc Lavier[1]

[1] Institute for Geophysics, Jackson School of Geosciences, University of Texas at Austin, Austin, Texas, USA.
[2] School of Geography, Environment and Earth Sciences, Victoria University of Wellington, Wellington, New Zealand.
[3] GNS Science, Lower Hutt, New Zealand.
[4] Faculty of Geosciences, Utrecht University, Utrecht, The Netherlands.

Contents of this file

Additional Supporting Information

Dataset S1

Introduction

The Supporting Information text further details GPS analysis and experimental friction methods, models, and supplementary results. Figures illustrate additional GPS modeling results, and provides a more detailed map with locations of samples tested in friction experiments. Tables provide GPS positions and velocities, GPS modeling inputs and results, fault rock sample descriptions and friction experiment results. Dataset S1 gives experimental friction laboratory results (see Text S6 for details).

Text S1. GPS uncertainty calculations

Formal uncertainties for GPS velocities, particularly from campaign observations, tend to underestimate their true uncertainty (e.g., Zhang et al., 1997; Williams et al., 2004). To correct for underestimated uncertainties, a random-walk noise component is commonly incorporated into the final uncertainties. This correction scales with the inverse of the square root of the observation period, given in Zhang et al. (1997) as:

$$\sigma_{RWN} = \frac{A_{RWN}}{\sqrt{T}} \tag{S1}$$

where T is the time series duration and A_{RWN} is the amplitude of the random walk noise. Following Koulali et al. (2015)'s study of Papua New Guinea GPS velocities, we use random walk noise increments of 0.3 mm/$\sqrt{\mathrm{yr}}$ for continuous sites and 1.0 mm/$\sqrt{\mathrm{yr}}$ for campaign sites. Formal and corrected uncertainties are shown in Table S2 columns 8-11.

Text S2. Earthquake offset corrections

Static elastic coseismic displacements due to far-field (~100 – 1,000 km) large earthquakes range from < 1 mm to 10's of mm (e.g., Banerjee et al., 2005; Tregoning et al., 2013) depending on the distance from the hypocenter, the regional crustal elastic stratification, the spatial distribution of slip, and slip characteristics such as rake and total slip (Pollitz et al., 1996). Tregoning et al. (2013) showed that M_w >8.0 earthquakes caused mm-scale offsets within ~1000 km of their epicenters. Correcting for such offsets is especially important in studies where the velocity signal of interest is small (mm-scale), as is the case for velocities across the Mai'iu fault. Therefore, we calculate coseismic corrections for all $M_w \geq 6.9$ (based on USGS catalogue magnitudes) earthquakes with hypocentral depths < 100 km located within 700 km of our Mai'iu fault network (Fig. 1) from 2008 to June 2018.

We use a spherical layered Earth model (Pollitz, 1996) of harmonic degree 1 to 1500 with PREM elastic stratification (Dziewonski & Anderson, 1981) to calculate surface displacements at our GPS sites due to uniform slip on prescribed fault source models. For the 2016 Mw 7.9 Solomon Islands earthquake (~725 km from our network), we use two fault planes to approximate the composite megathrust source model of Lee et al. (2018), which matches observed teleseismic waveforms better than other proposed source models. This source model ascribes all coseismic slip to patches of the curved subduction megathrust and hence predicts larger horizontal displacements at our GPS sites than source models with rupture of an intraslab fault (Lay et al., 2017; USGS finite fault model). We find that surface displacements predicted by the model of Lee et al. (2018) best match those estimated from time-series analysis of continuous GPS data from site PNGM, the nearest continuous GPS site with similar azimuth to the hypocenter as our sites.

For other nearby 2008-2018 $M_w \geq 6.9$ earthquakes (~350 – 825 km from our network), we approximate the USGS finite fault models (Hayes, 2017; U.S. Geological Survey, 2019) as finite planes with uniform slip. For the few events without published finite fault models, we estimate slip planes based on hypocentral depth, focal mechanism solutions, regional tectonics and nearby event characteristics constrained by typical subduction zone earthquake length-width ratios from Strasser et al. (2010), as most of these events were subduction thrust events near the New Britain and San Cristobal trenches. The earthquake closest to our network was the 2010 M 6.9 New Britain event (~350 km away), while the earthquake with the largest static coseismic offsets at our sites was the 2016 M 7.9 New Britain event (~700 km away). We also reevaluate and correct for coseismic offsets due to the 2 April 2007 M_w 8.1 Solomon Islands earthquake using the coseismic slip model of Wallace et al. (2015), which was developed by jointly inverting horizontal GPS displacements and vertical displacements from coral paleogeodetic observations in the Solomon Islands (Taylor et al., 2008) (Fig. S2). All slip models are tuned to approximately match the seismologically inferred M_w using a shear modulus of 25 GPa, and the details of each are listed in Table S3. GPS positions are corrected by adding static offset corrections equal and opposite to the modeled coseismic offsets during the GLOBK stage of processing.

Text S3. Block modeling (TDEFNODE)

Using the preferred block and fault configuration (Figures 2a, S3; Table S5), we perform inversions with different constraints on fault locking to explore how model constraints influence preferred locking distributions and data misfits. For example, the best-fit model (Figure 2) results from inversions where the coupling ratio (Φ) is required to decrease with increasing depth for all faults. We also test models where Φ is free to increase or decrease with depth (Figure S4a), as well as models where the Mai'iu fault is prescribed to be fully creeping (Φ = 0) or fully locked (Φ = 1) at all depths (Figures S4b, S4c, respectively), or fully locked at the surface (Figure S4d) or from the surface to 2, 4, 9, or 14 km depth (Figures S4e, S4f, S4g, S4h, respectively).

Text S4. Dislocation modeling of vertical velocities

Vertical velocities can also be valuable for investigating fault locking processes (e.g., Segall, 2010). However, because horizontal displacements are larger than vertical displacements for LANFs and vertical GPS uncertainties are typically 3–5 times larger than horizontal ones (e.g., Bennett et al., 2007; Serpelloni et al., 2013), we first consider only the strike-perpendicular horizontal velocities. Vertical velocities also suffer from an indeterminate reference frame problem and can be influenced by regional-scale uplift or subsidence processes unrelated to fault slip. Horizontal velocities can be tied to the rigid block motion of adjacent crustal blocks to isolate the components related to fault slip or locking. To address these issues, some authors select the site least likely to be affected by vertical tectonic motions and use its vertical velocity as the vertical reference frame (e.g., Beavan et al., 2010). Even with this method and high-precision continuous GPS observations, it is necessary to arbitrarily adjust all velocities by a baseline value in order to compare them to analytical physical models of crustal deformation (Beavan et al., 2010).

Vertical velocities across the fault show a sharp change on the order of 5 mm/yr from subtle footwall subsidence to hanging wall uplift near the fault trace, decaying to hanging wall subsidence with distance from the trace. At face value, the wavelength of vertical velocity change across the hanging wall suggests deeper locking than the horizontal velocities alone. Including both horizontal and vertical velocities, the best-fit ($\chi^2 = 2.41$) model fault dips 32° and slips at 13.5 mm/yr below a locking depth of 13 km. However, addressing the vertical reference frame ambiguity by allowing for a uniform modeled vertical velocity shifts across all sites of -5 to +5 mm/yr leads to a best-fit ($\chi^2 = 1.53$) model fault dipping 28° and slipping 10 mm/yr below a locking depth of 3 km, similar to the best-fitting model from horizontal velocities alone, with -3 mm/yr uniform vertical velocity shift.

Text S5. Quantitative X-ray diffraction methods

Eight fault rock samples (Table S4) were analyzed by X-Ray Diffraction by Mark Raven at CSIRO Land and Water Flagship, Mineral Resources Flagship, at the Centre for Australian Forensic Soil Science (CAFSS), in Urrbrae, South Australia. From these samples, 1.5 g sub-samples were ground for 10 minutes in a McCrone micronizing mill under ethanol. The resulting slurries were oven dried at 60 °C then thoroughly mixed in an agate mortar and pestle before being lightly pressed into aluminum sample holders for X-ray diffraction analysis. XRD patterns from the micronized materials showed variable hydration of the interlayer which causes problems with quantification. Because the samples did not appear to contain any water-soluble phases, they were calcium saturated, and the data were re-analyzed. XRD patterns were recorded with a PANalytical X'Pert Pro Multi-purpose Diffractometer using Fe filtered Co Ka radiation, auto divergence slit, 2° anti-scatter slit and fast X'Celerator Si strip detector. The diffraction patterns were recorded in steps of 0.016° 2θ with a 0.4 second counting time per step, and logged to data files for analysis. XPLOT and HighScore Plus (PANalytical) search and match software were used to perform qualitative analysis. The abundance of identified mineral phases was then determined using SIROQUANT software from Sietronics Pty Ltd. Results are normalized to 100% and do not include unidentified or amorphous phases. Table S4 lists each sample's mineral phases and their relative proportion.

Text S6. Hydrothermal Friction Experiments

Complete hydrothermal friction results can be found in Supplementary Dataset S1. The text file contains data in tab delimited columns arranged by experiment (see Table S7 for experiment details). Lower case "d" denotes displacement (mm) and μ denotes the corrected coefficient of friction. Acquired raw torque and normal force data were processed to obtain shear stress and normal stress measurements respectively. Raw, externally measured, torque data were corrected for fluid pressure and shear displacement-dependent friction of the Teflon-coated O-ring seals using calibration values obtained in runs with a dummy sample of carbon-coated PolyEtherEtherKeton with a known sliding friction; seal friction is typically around 0.03 kN (equivalent to ~1.5 MPa shear stress). The contribution of the Molykote-coated confining rings to the measured friction is negligible (see also den Hartog et al., 2012a). The applied normal stress was corrected for the stress supported by the internal seals, the level of which is clearly visible during initial loading and was generally around 0.5 kN (equivalent to ~2 MPa normal stress acting on the sample).

In general, most fault gouges strengthen with increasing simulated depth (i.e. increasing temperature, effective normal stress, and fluid pressure) during an individual experiment. In some experiments, strengthening is the result of a long-term displacement-dependent increase in friction (e.g. Figure 5c), whereas in other experiments strengthening is abrupt and is the result of increased simulated depth (e.g. Figure 5b). The repeat experiment pairs u368+u370, u369+u371 and u546+u547 (note that a different velocity profile was applied in experiments u368 and u369) show good reproducibility in terms of the general evolution of friction with displacement, the level of friction and the velocity dependence of friction. Variability in friction is less than 0.05 in all cases and less than 0.02 in most cases. Unstable sliding (stick-slips) is encountered in only a few experiments, typically at a temperature range between 250 °C and 350 °C at low sliding velocity (< 30 μm/s) for samples with a friction coefficient of at least 0.6 (Figures 5b,d). Some history dependence (i.e. displacement dependence) is seen in the experiments performed at the highest temperatures (i.e., 300-350-400-450 °C), in which the first series of velocity steps reproduces the temperature conditions of the last series of velocity steps performed in the low temperature experiment (Table S7). The friction coefficient recorded at low displacements at 300°C is consistently lower than that recorded at high displacements at 300 °C, except for experiment u775. It should be noted that both effective normal stress and fluid pressure are considerably lower in the low-displacement 300 °C steps (120 vs. 180 MPa and 80 vs. 180 MPa, respectively), which might explain the difference.

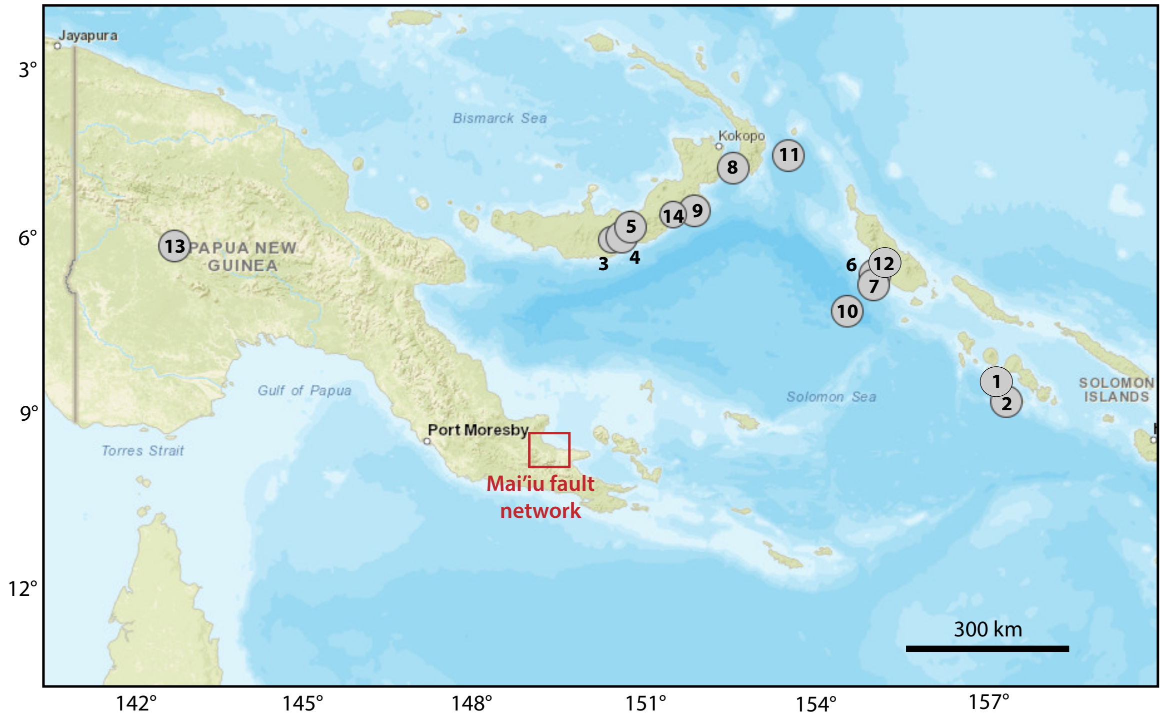

Figure S1. Regional earthquakes of M ≥ 6.9 corrected for using STATIC1D (Text S2; U.S. Geological Survey, 2019). See Table S2 and Text S2 for a list and description of these events. Labeled numbers refer to event numbers in Table S2.

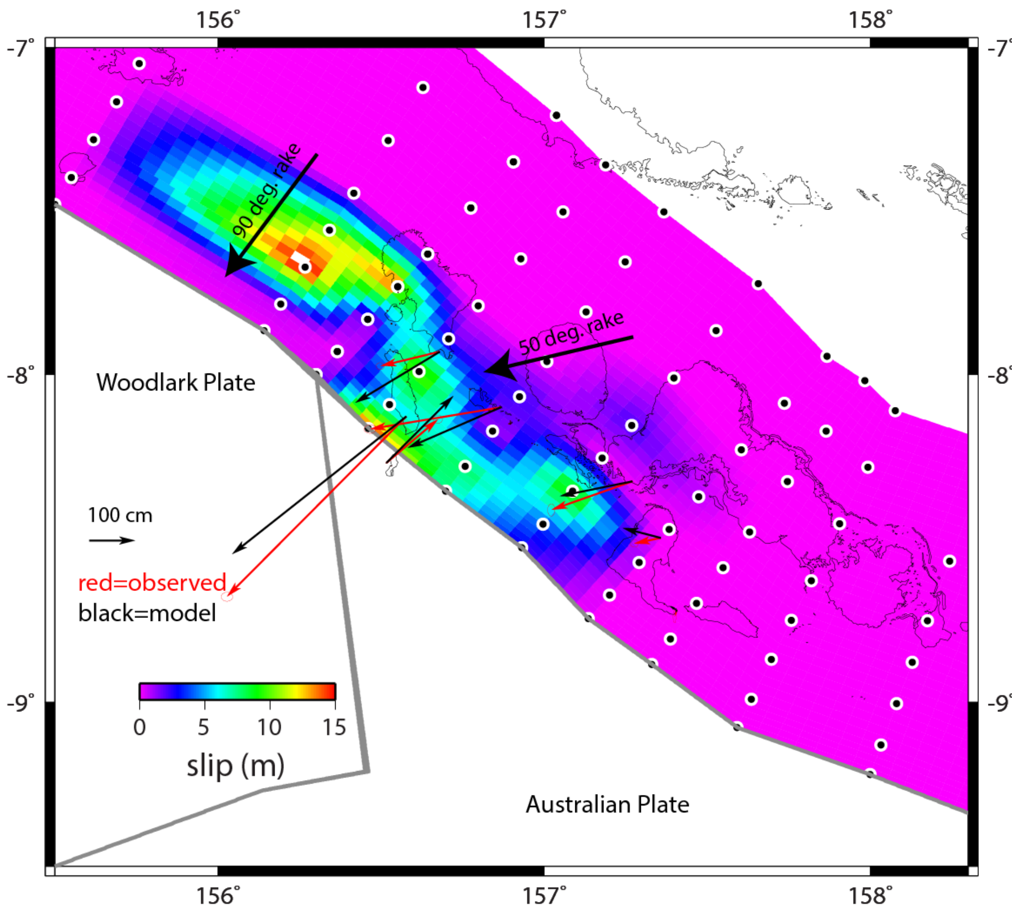

Figure S2. Slip distribution for the 2007 M 8.1 Solomon Islands earthquakes from joint inversion of campaign GPS displacements (red vectors) and coastal uplift/subsidence recorded by coral reef platforms (Wallace et al., 2015). Black vectors show the modeled fit to the horizontal component of GPS velocities. Larger black vectors show the rake of slip.

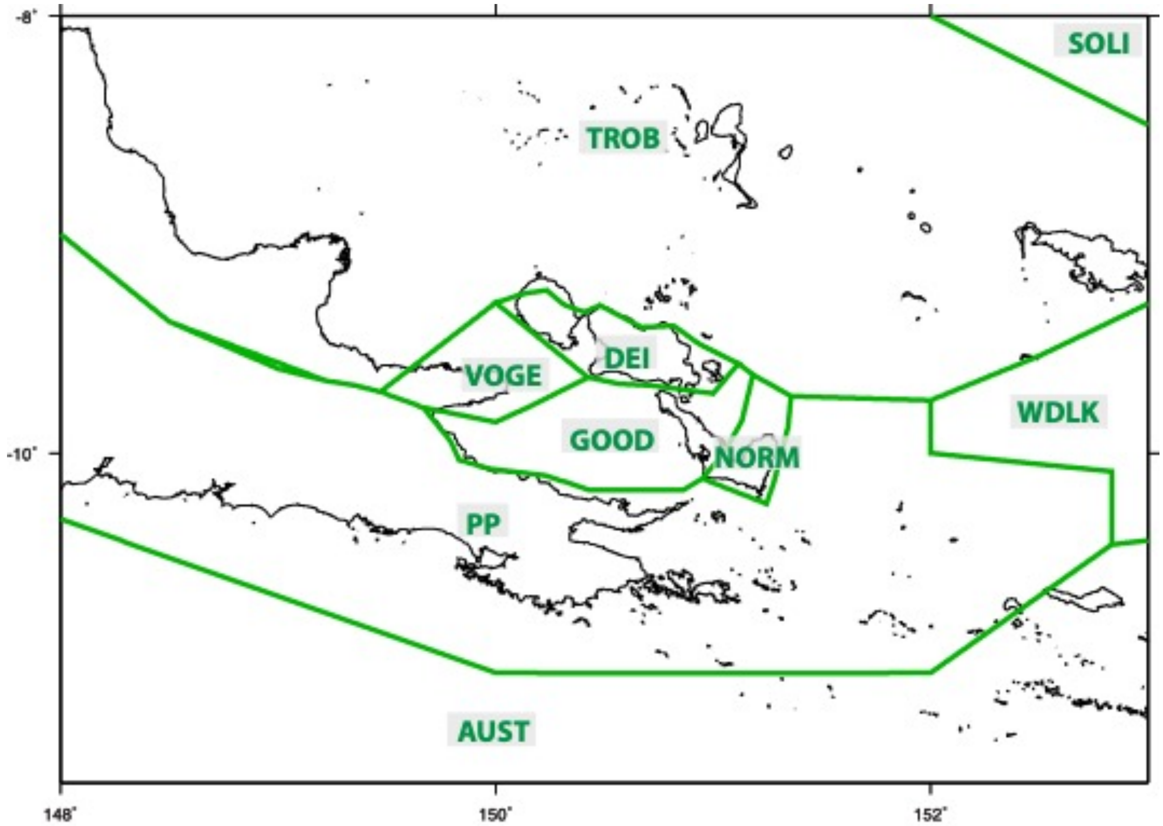

Figure S3. Individual blocks tested for independence. *F* tests cannot statistically distinguish between models where VOGE and GOOD are considered individual blocks and ones where they are one unified block (Table S5). Therefore, we treat them as one block in subsequent TDEFNODE block models (configuration 2 in Table S5). TROB = Trobriand Islands block; SOLI = Solomon Islands block; WDLK = Woodlark Plate block; DEI = D'Entrecasteaux Islands block (Goodenough & Fergusson Islands); NORM = Normanby Island block; VOGE = Cape Vogel block; GOOD = Goodenough Basin block; PP = Papuan Peninsula block; AUST = Australian Plate block.

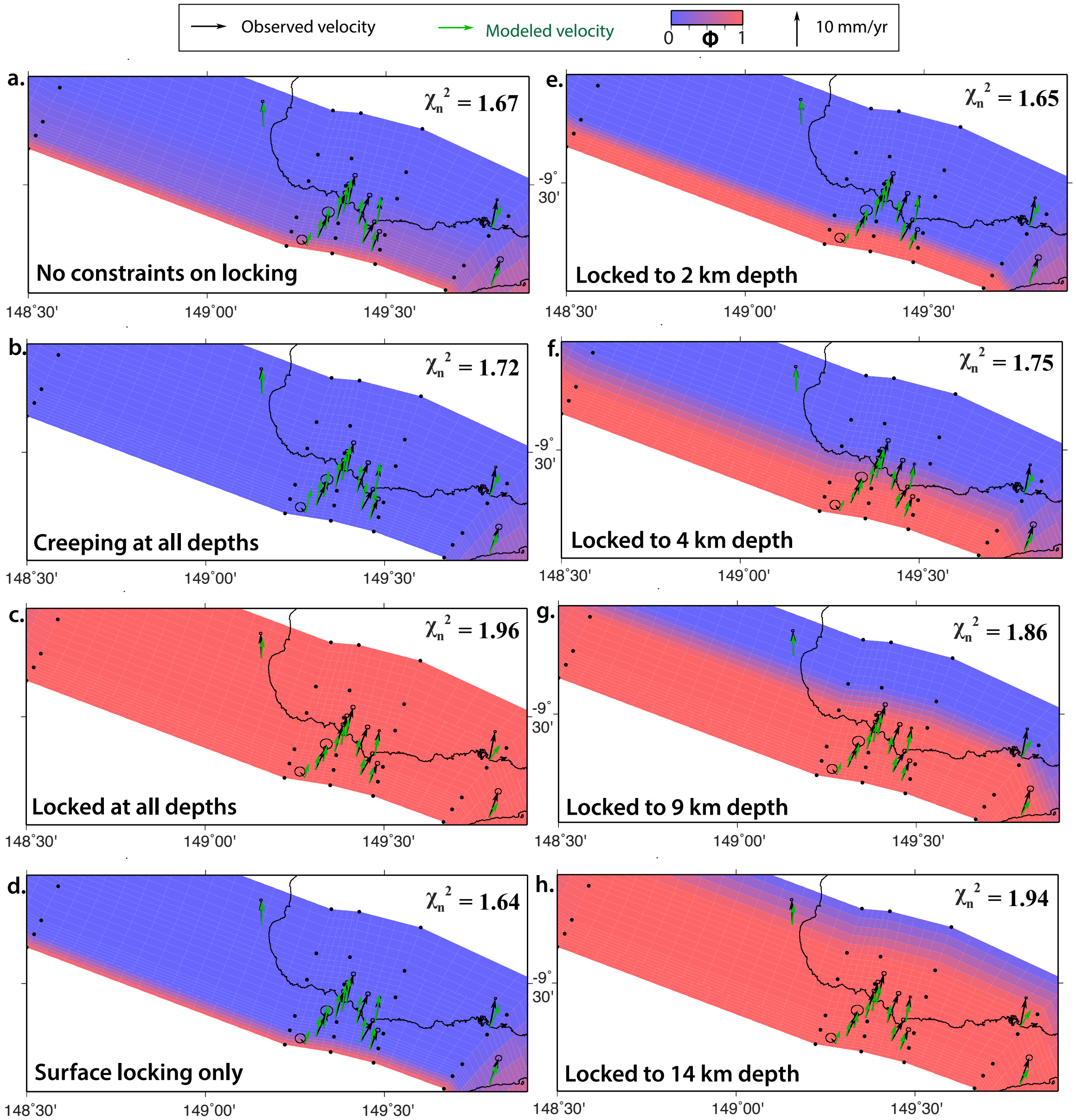

Figure S4. Mai'iu fault locking results for different inversion constraints and locking depths in the elastic block models. We test models where the kinematic coupling ratio, Φ, is free to increase or decrease with depth (a), as well as models where the Mai'iu fault is prescribed to be fully creeping (Φ = 0) or fully locked (Φ = 1) at all depths (b, c, respectively), or fully locked at the surface (d) or from the surface to 2, 4, 9, or 14 km depth (e, f, g, h, respectively).

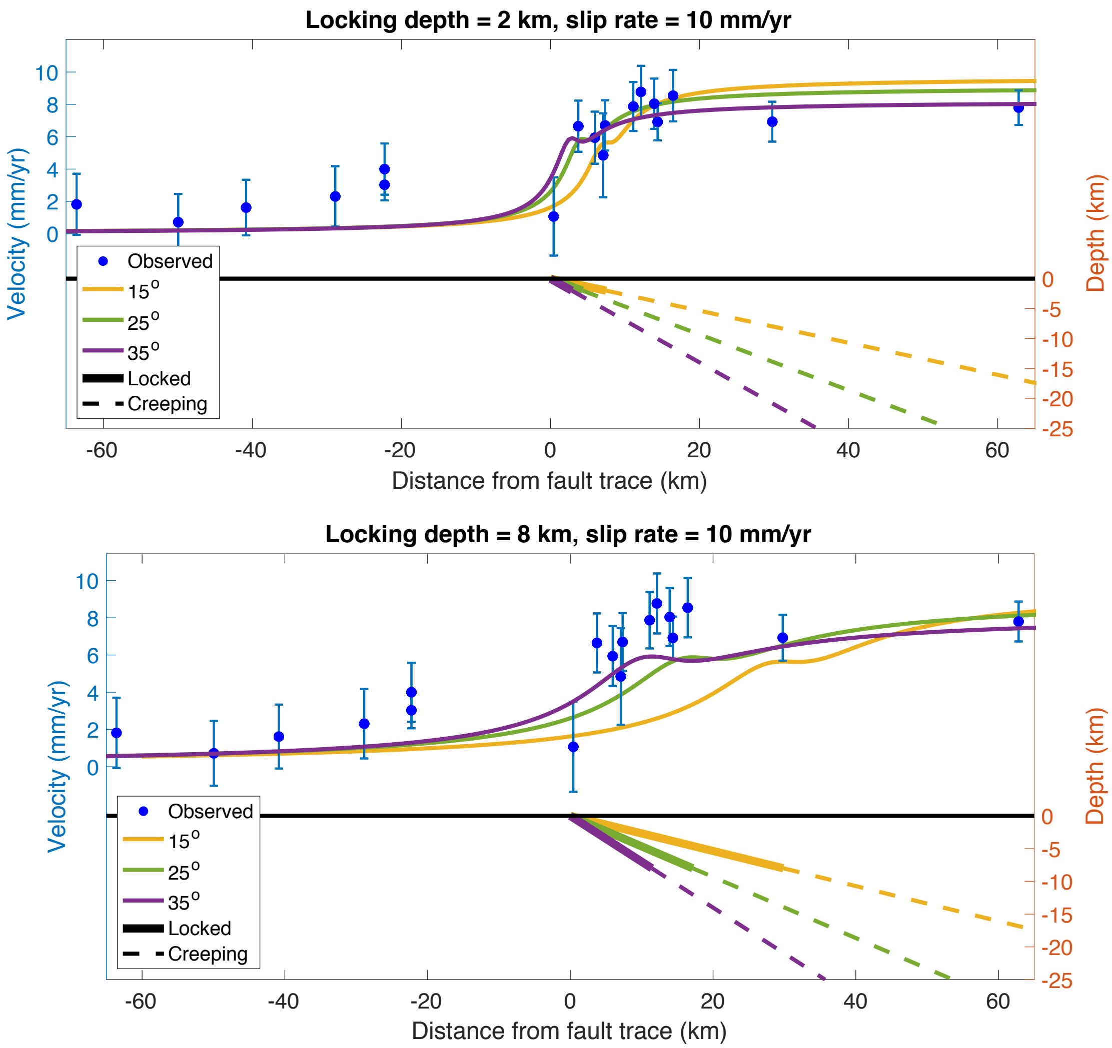

Figure S5. Illustrated example of tradeoffs between locking depth, fault dip and predicted velocities for planar dislocation models with locking at the surface. Observed velocities are parallel to profile X-X' of Fig. 2a and are relative to a fixed Australian plate. Fault dip has less effect on velocities for shallowly locked faults than for more deeply locked faults.

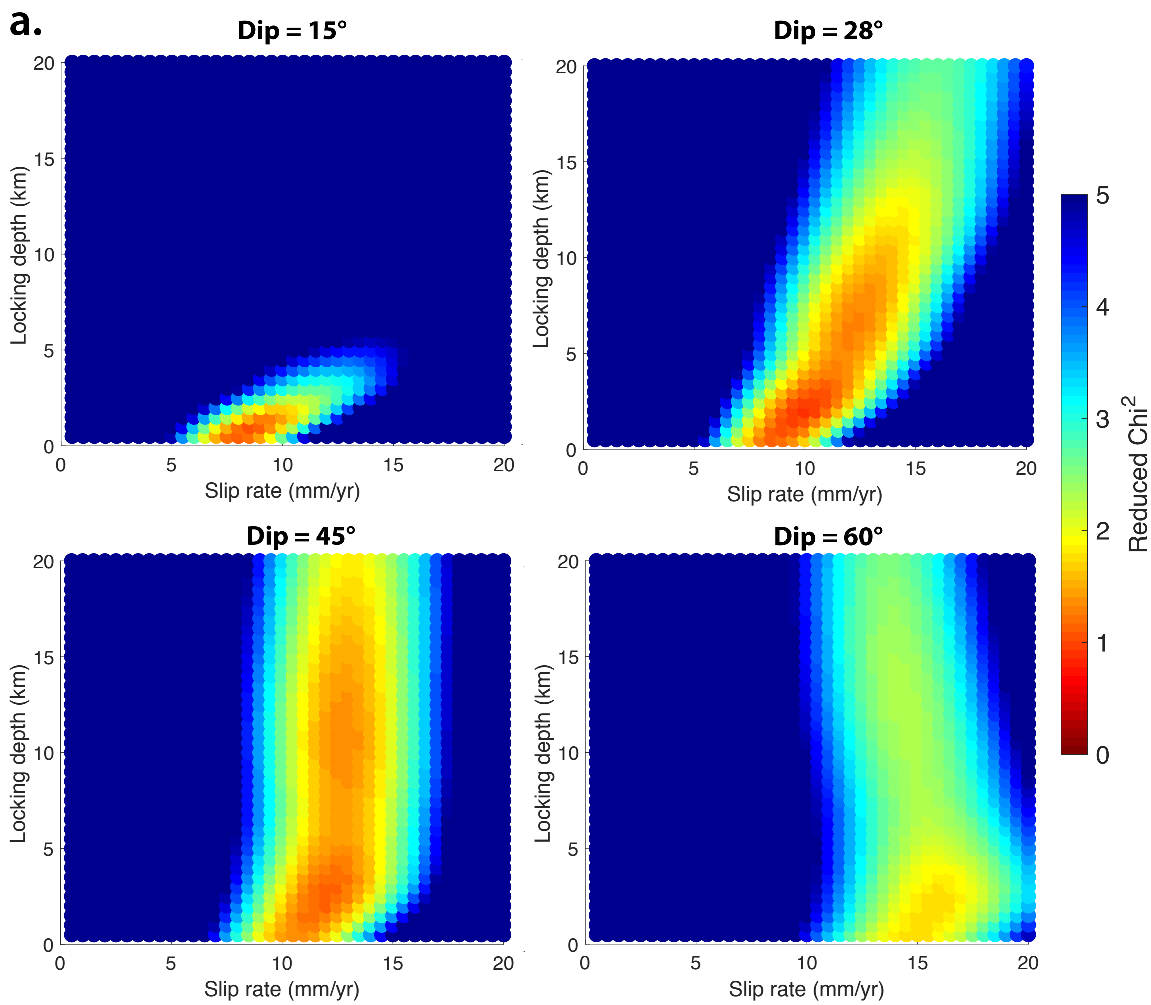

a.
Dip = 15°
Dip = 28°
Dip = 45°
Dip = 60°
Locking depth (km)
Slip rate (mm/yr)
0
5
10
15
20
Reduced Chi^2
0
1
2
3
4
5

b.

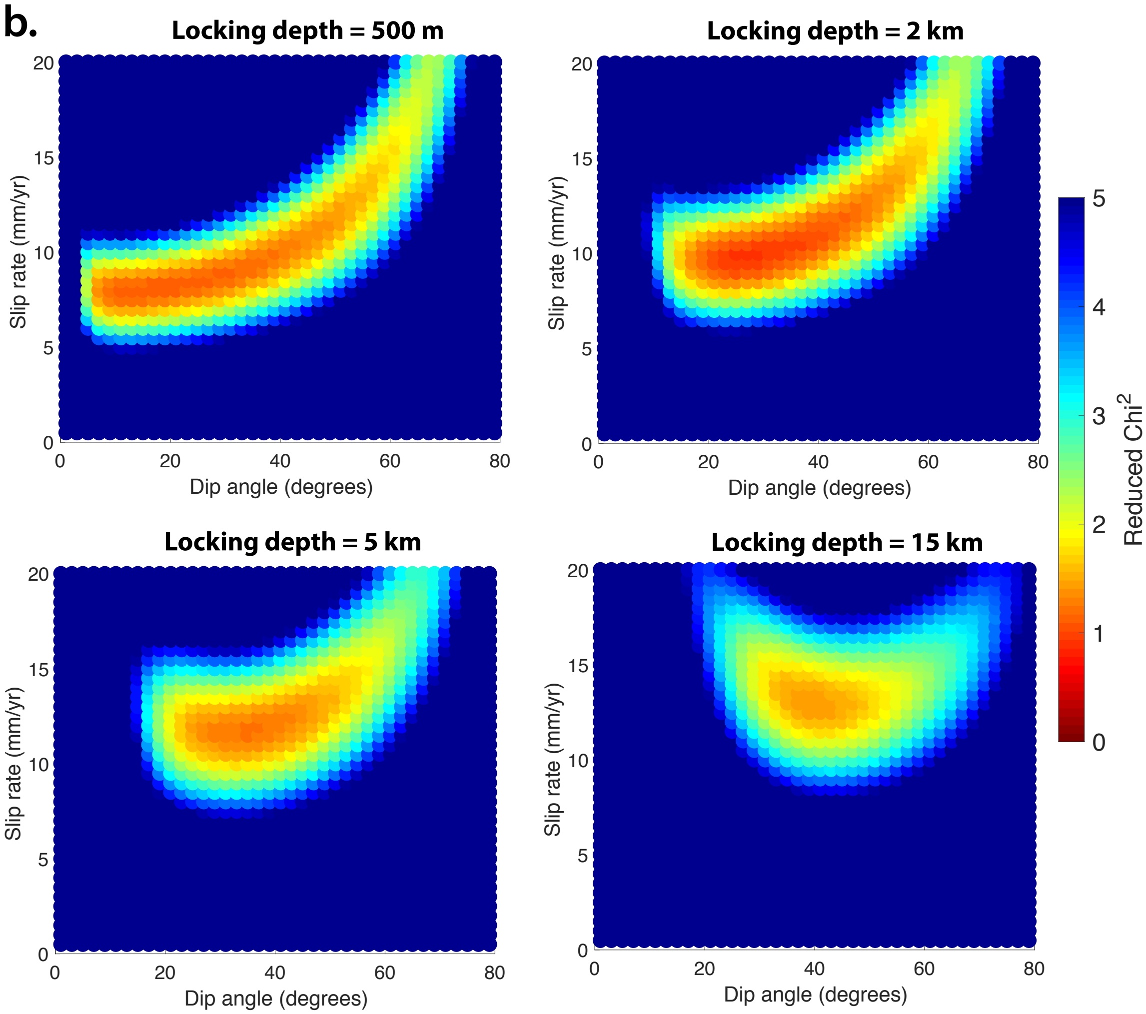
Locking depth = 500 m
Locking depth = 2 km
Locking depth = 5 km
Locking depth = 15 km
Slip rate (mm/yr)
Dip angle (degrees)
0
5
10
15
20
0
20
40
60
80
Reduced Chi^2
0
1
2
3
4
5

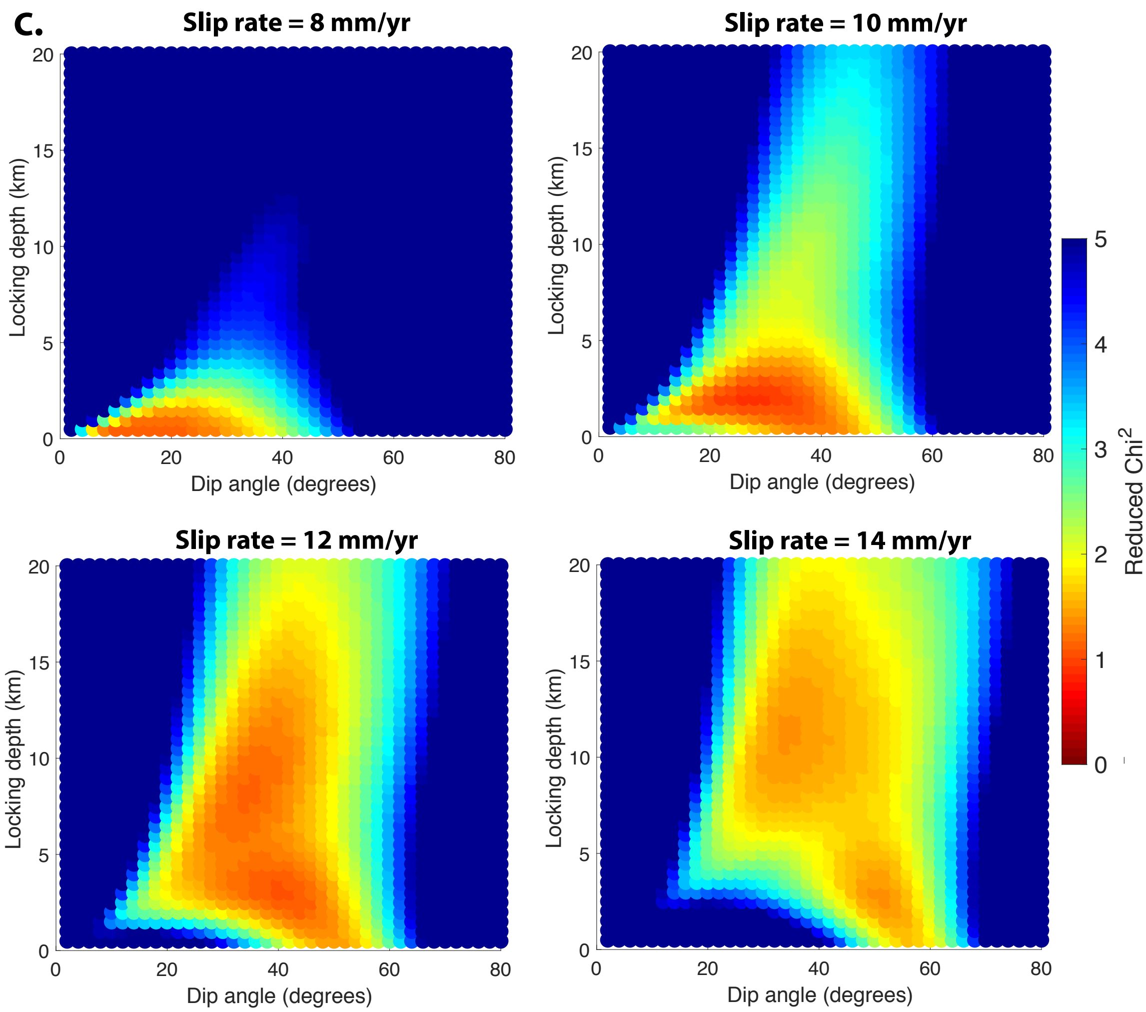

Figure S6. Parameter sensitivity plots for locked-to-surface dislocation models showing data misfit (reduced χ^2) tradeoffs between: a.) slip rate and locking depth for dips of 15°, 28°, 45°, and 60°; b.) dip angle and slip rate for locking depths of 0.5, 2, 5, and 15 km; c.) dip angle and locking depth for slip rates of 8, 10, 12, and 14 mm/yr.

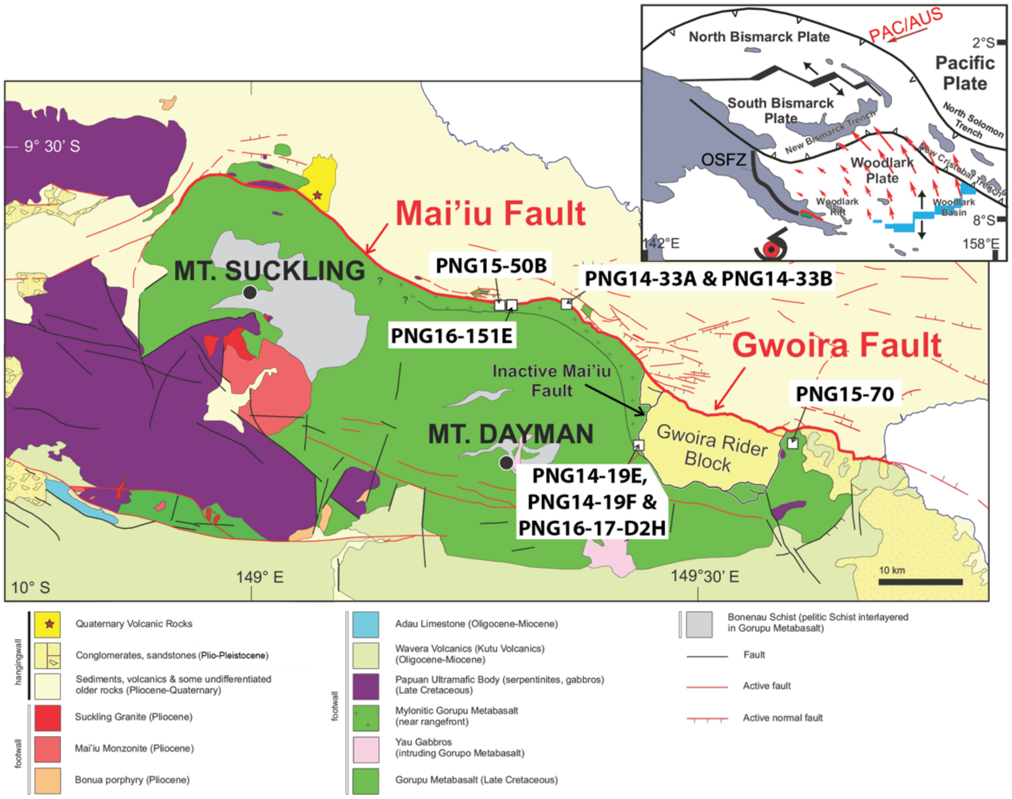

Figure S7. Tectonic setting (inset) and geological map showing the active and inactive strands of the Mai'iu Fault and the location of the fault rocks analyzed. Each fault rock is identified by its field sample number. Map after Little et al. (2019) and Mizera et al (2020).

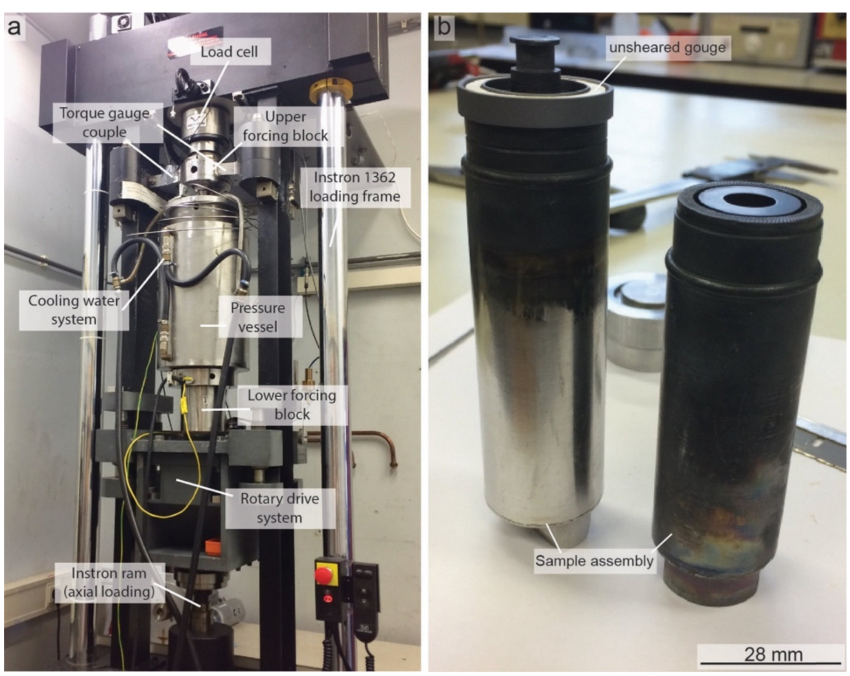

Figure S8. Images of the High Temperature and Pressure (HPT) Lab, Utrecht University, hydrothermal ring shear apparatus used to measure the frictional properties of Mai'iu fault rock samples. (a) is a labelled photograph of the apparatus, and (b) depicts the two pistons which, fitted together with an annulus of gouge between them, are inserted into the pressure vessel and sheared under controlled conditions of temperature, effective normal stress, and velocity.

Site	2002	2004	2005	2006	2008	2009	2010	2012	2015	2016	2018
AGAN									x		x
ALT2	x	x				x	x	x			
BASM						x	x	x			
BAYA						x	x	x	x		
BINI									x	x	x
BORO									x	x	x
BWAR						x	x	x			
DAIO						x	x	x			
DARB						x	x	x			
DD01									x	x	
DIGA						x	x	x			
ESAA		x			x		x	x			
GIWA						x	x	x			
GONO									x	x	x
GOUR									x	x	x
GUA1		x					x				
GUMA						x	x	x			
HEHE						x	x	x			
JONE						x	x	x			
KABU									x	x	
KALO						x	x	x			x
KAWA						x	x	x			
KEIA						x	x	x			
KIBU									x	x	x
KILI						x	x	x			x
KURA						x	x	x			
KWAN						x	x	x			
KWAT						x	x	x			
LELE						x	x	x			
LOS2		x					x	x			
MAAP						x	x	x			
MENA						x	x	x			
MORA						x	x	x			x
MORB									x	x	x
NUBE						x	x	x			
PEMM						x	x	x		x	
RAB2							x				x
RABA						x	x	x			x

RAKO									x	x	x
SALM		x				x	x	x			
SIBA						x	x	x			
SIRI						x	x	x			
SMRI						x	x	x			
STRA						x	x	x			
TUF2						x	x	x	x		x
TUFI		x	x	x							
UAMA						x	x	x			
VAKU						x	x	x			
VIVI					x		x				
WAIB						x	x	x			x
WANI						x	x	x		x	
WAPO						x	x	x			
WATL		x			x		x	x			
YAMS									x	x	
YANA						x	x	x			

Table S1. GPS sites and observation years used in this study.

Site	Longitude	Latitude	V_N^{IT14}	V_E^{IT14}	V_N^{AUS}	V_E^{AUS}	σ_N^f	σ_E^f	σ_N^{rwn}	σ_E^{rwn}
	°	°	mm/yr	mm/yr	mm/yr	mm/yr	mm/yr	mm/yr	mm/yr	mm/yr
AGAN	149.387	-9.93	34.21	59.4	3.90	1.01	0.63	0.74	1.20	1.31
ALT2	150.338	-10.31	35.05	57.54	2.41	2.20	0.14	0.16	0.45	0.47
BASM	150.833	-9.466	34.85	68.54	13.60	1.66	0.76	0.87	1.33	1.44
BAYA	149.474	-9.608	34.6	62.4	6.93	1.26	0.23	0.27	0.63	0.67
BINI	149.308	-9.648	36.19	61.57	6.04	2.84	0.61	0.73	1.20	1.32
BORO	149.459	-9.684	35.57	60.97	5.50	2.27	0.64	0.78	1.23	1.37
BWAR	151.185	-9.94	36.04	58.13	3.34	3.15	0.88	1.00	1.46	1.58
DAIO	150.427	-10.408	34.12	57.06	1.96	1.34	1.08	1.25	1.65	1.82
DARB	151.015	-9.927	33.86	57.98	3.12	0.93	0.97	1.06	1.55	1.64
DD01	149.289	-9.835	35.91	54.54	-1.00	2.65	1.60	1.88	2.57	2.85
DIGA	151.204	-10.2	34.67	58.42	3.63	1.91	1.53	1.55	2.11	2.13
ESAA	150.812	-9.739	37.41	59.87	4.93	4.35	0.34	0.42	0.70	0.78
GIWA	149.794	-9.78	35.74	62.69	7.35	2.54	1.12	1.33	1.70	1.91
GONO	149.434	-9.661	36.73	61.35	5.87	3.41	0.56	0.68	1.15	1.27
GOUR	149.362	-9.597	35.69	63.05	7.54	2.33	0.51	0.61	1.10	1.20
GUA1	152.944	-9.225	36.57	83.52	29.47	3.58	0.37	0.45	0.77	0.85
GUMA	150.865	-9.21	32.55	70.84	15.92	-0.76	0.80	0.93	1.38	1.51
HEHE	150.874	-10.226	34.28	58.02	3.10	1.48	1.07	1.27	1.65	1.85
JONE	150.102	-10.095	34.97	58.02	2.79	1.97	0.77	0.87	1.34	1.44
KABU	149.33	-9.624	34.24	60.38	4.86	0.89	2.05	2.64	3.07	3.66
KALO	150.43	-9.414	34.54	63.94	8.84	1.26	0.22	0.24	0.55	0.57
KAWA	150.299	-8.522	26.69	69.17	14.02	-7.05	0.96	1.07	1.53	1.64
KEIA	150.554	-10.213	34.66	57.22	2.17	1.80	0.83	0.93	1.40	1.50
KIBU	149.381	-9.577	34.9	63.53	8.03	1.53	0.57	0.68	1.16	1.27
KILI	150.292	-9.496	34.91	63.94	8.79	1.65	0.23	0.26	0.56	0.59
KURA	151.036	-10.11	34.59	56.13	1.28	1.76	1.10	1.09	1.68	1.67
KWAN	151.274	-9.923	33.01	58.92	4.16	0.12	0.88	1.05	1.46	1.63
KWAT	150.712	-9.311	32.68	70.48	15.50	-0.61	0.72	0.80	1.30	1.38
LELE	150.728	-10.302	33.53	55.36	0.38	0.75	0.93	1.04	1.50	1.61
LOS2	151.125	-8.535	28.31	72.08	17.26	-5.30	0.25	0.31	0.61	0.67
MAAP	150.4374	-9.6104	35.55	62.5	7.41	2.37	0.39	1.12	1.18	1.70
MENA	149.936	-9.757	34.91	62.25	6.96	1.72	1.01	1.13	1.59	1.71
MORA	150.187	-9.432	33.51	64.14	8.95	0.20	0.22	0.24	0.55	0.57
MORB	149.422	-9.61	36.56	63.65	8.16	3.21	0.63	0.79	1.22	1.38
NUBE	149.867	-10.399	33.91	55.7	0.38	1.03	0.90	0.99	1.47	1.56
PEMM	149.795	-9.621	34.84	63.35	8.01	1.56	0.27	0.32	0.65	0.70
RABA	149.834	-9.972	35.44	58.79	3.46	2.34	0.10	0.12	0.37	0.39
RAKO	149.393	-9.557	35.43	63.86	8.36	2.05	0.61	0.75	1.20	1.34

SALM	150.796	-9.663	37.72	65.59	10.64	4.62	0.21	0.24	0.57	0.60
SIBA	150.268	-10.684	32.83	57.05	1.89	0.16	1.24	1.18	1.81	1.75
SIRI	149.708	-9.841	36.52	58.04	2.66	3.33	1.34	1.42	1.92	2.00
SMRI	150.662	-10.613	32.96	56.62	1.62	0.32	0.87	0.93	1.44	1.50
STRA	151.868	-10.225	34.72	58.69	4.18	2.09	0.82	0.90	1.40	1.48
TUF2	149.318	-9.079	32.1	63.18	7.65	-1.52	0.23	0.25	0.56	0.58
TUFI	149.323	-9.08	30.51	63.96	8.44	-3.10	0.95	1.09	1.65	1.79
UAMA	150.953	-9.452	33.38	70.92	16.03	0.20	1.16	1.35	1.73	1.92
VAKU	151.184	-8.853	30.03	72.51	17.72	-3.42	0.66	0.73	1.23	1.30
VIVI	150.324	-9.31	33.28	64.98	9.84	-0.07	0.97	1.12	1.68	1.83
WAIB	150.139	-9.245	33.73	66.61	11.40	0.32	0.24	0.26	0.57	0.59
WANI	149.157	-9.338	33.34	62.52	6.93	-0.18	0.35	0.42	0.73	0.80
WAPO	150.532	-9.355	32.76	69.06	14.00	-0.53	1.12	1.31	1.70	1.89
WATL	150.243	-9.211	32.89	66.21	11.04	-0.52	0.35	0.43	0.71	0.79
YAMS	149.279	-9.7	31.93	57.23	1.69	-1.41	2.18	2.50	2.77	3.09
YANA	151.897	-9.271	33.51	74.89	20.39	0.38	1.00	1.20	1.59	1.79

Table S2. Coordinates, velocities, and uncertainties for each GPS site. $\mathbf{V_N^{IT14}}$ and $\mathbf{V_E^{IT14}}$ are the North and East components of velocity in the ITRF14 reference frame. $\mathbf{V_N^{AUS}}$ and $\mathbf{V_E^{AUS}}$ are the North and East components of velocity relative to the Australian Plate. $\boldsymbol{\sigma}_\mathbf{N}^\mathbf{f}$ and $\boldsymbol{\sigma}_\mathbf{E}^\mathbf{f}$ are the formal uncertainties for the North and East velocity components. $\boldsymbol{\sigma}_\mathbf{N}^\mathbf{rwn}$ and $\boldsymbol{\sigma}_\mathbf{E}^\mathbf{rwn}$ are the uncertainties of the North and East velocity components after correcting for random-walk noise (Text S1).

Plate	Longitude	Latitude	Rotation Rate	Major Axis Uncertainty	Minor Axis Uncertainty	Orientation of Major Axis
	(°)	(°)	(°/Myr)	(Distance in °)	(Distance in °)	(° East of North)
WDLK	148.92	-10.97	2.81 ± 0.40	0.77	0.19	82
TROB	147.75	-9.33	2.67 ± 0.23	0.42	0.19	75
DEI	147.90	-8.95	2.04 ± 1.11	1.93	0.34	104
GOOD	175.79	-18.84	-0.16 ± 1.00	102.36	3.54	107
NORM	150.42	-9.70	1.64 ± 0.28	0.68	0.52	151
PP	149.23	-9.40	0.73 ± 0.28	0.91	0.6	128

Plate	Ω_x	Ω_y	Ω_z	σ_x	σ_y	σ_z	cov(x,y)	cov(x,z)	cov(y,z)
WDLK	-2.36	1.43	-0.54	0.35	0.18	0.07	-0.0646	0.0255	-0.0132
TROB	-2.23	1.41	-0.43	0.20	0.11	0.03	-0.021	0.0066	-0.0036
DEI	-1.71	1.07	-0.32	0.95	0.54	0.18	-0.5127	0.1745	-0.0998
GOOD	0.15	-0.01	0.05	0.96	0.55	0.19	-0.5264	0.1775	-0.102
NORM	-1.41	0.80	-0.28	0.24	0.14	0.05	-0.0329	0.0125	-0.0072
PP	-0.62	0.37	-0.12	0.24	0.14	0.05	-0.0331	0.0119	-0.0069

Table S3. Poles of rotation of crustal blocks relative to the Australian Plate. Cartesian coordinates are shown in the lower section. Ω_x, Ω_y, and Ω_z are the Cartesian angular velocity vector components; σ_x, σ_y, and σ_z are the uncertainties of the respective components. The final columns give the covariances of component pairs. WDLK = Woodlark Plate; TROB = Trobriand Block; DEI = D'Entrecasteaux Islands block; GOOD = Goodenough Bay block; NORM = Normanby Island block; PP = Papuan Peninsula block.

#	Year	Event name	d_h	Lat.	Lon.	d_1	d_2	Str.	Dip	L	Rake	Slip	dE	dN	D
			km	°	°	km	km	°	°	km	°	m	mm	mm	km
1	2007	M 8.1 Solomon Isl.	24*												
2	2010	M 7.1 Solomon Isl.	10	-8.67	157.30	5	15	326	15	45	94	0.8			
3	2010	M 6.9 New Britain 1	28	-6.37	150.35	25	45	185	50	45	75	0.6			
4	2010	M 7.3 New Britain	35	-6.00	150.20	25	35	257	24	70	102	1.2			
5	2010	M 7.0 New Britain	44	-5.70	150.65	16	40	240	31	60	60	0.25			
6	2014	M 7.1 Bougainville 1	61	-6.39	154.97	50	75	310	45	50	80	0.7			
7	2014	M 7.5 Bougainville	43	-6.36	154.90	15	45	315	33	49	95	1.5			
8	2015	M 7.5 New Britain 1	41*												
		Segment 1		-5.40	152.25	12	17	252	44	120	61	0.3			
		Segment 2		-5.19	152.91	17	28	252	33	120	90	0.8			
		Segment 3		-5.08	152.16	28	43	252	24	120	65	0.5			
		Segment 4		-4.80	152.64	43	57	252	13	40	90	0.3			
9	2015	M 7.5 New Britain 2	55	-5.38	151.71	26	56	244	29	70	65	1			
10	2015	M 7.1 Bougainville 2	10	-7.54	154.87	0	16	125	67.5	80	270	1.2			
11	2016	M 7.9 New Britain 1	95*										7.90	7.62	725
		Segment 1		-5.00	153.00	0	50	313	27.9	260	90	1			
		Segment 2		-4.50	153.50	50	100	313	65	100	90	1			
12	2017	M 7.9 Bougainville	135	-6.70	155.20	136	166	135	55	50	90	8	3.16	1.98	750
13	2018	M 7.5 Highlands	25	-5.80	142.20	1	30	308	33	100	90	1	0.02	0.03	825
14	2018	M 6.9 New Britain 2	35	-5.82	151.07	25	45	244	45	45	82	0.6	0.04	0.55	500

Table S4. Events and fault parameters used in regional earthquake corrections, based on USGS finite fault models (U.S. Geological Survey, 2019). Latitude and longitude are given for the lower corner of the fault farthest along the strike direction. d_h is the hypocentral depth. d_1 and d_2 are the upper and lower depths of the fault, respectively. Str is the fault strike. L is the along-strike length of the slipping fault and slip is the total slip. For the events from 2016-2018 (during our Mai'iu fault campaign experiment), D is the approximate distance from the earthquake to our GPS sites near the Mai'iu fault, dE is the average magnitude of the eastward offset at our campaign sites due to each event, and dN is the average magnitude of the northward offset at our campaign sites due to each event. Red events had no available USGS finite fault model as of publication. * = events with non-planar or multi-segment sources (Text S2). Individual fault segment parameters are listed below these events, except for the 2007 Solomon Islands earthquake, for which the modeled slip distribution from Wallace et al. (2015) is shown in Fig. S2.

Config.	Description	N_{data}	N_{params}	DOF	χ^2	*F* test probability	Is (1) better?
1	Best fit	255	46	209	1.65		
2	VOGE + GOOD	255	43	212	1.69	57	No
3	VOGE + DEI + GOOD	255	39	216	1.93	87	Probably
4	GOOD + NORM	255	42	213	2.02	93	Probably
5	GOOD + NORM + DEI	255	38	217	1.95	89	Probably
6	DEI + TROB	255	38	217	1.82	76	Probably

Table S5. Results of *F* test for block independence based on GPS velocities in Table S2 and block boundary configurations in Figure S3. N_{data} = number of data; N_{params} = number of free parameters; DOF = degrees of freedom. 'VOGE + DEI + GOOD' refers to models where Cape Vogel (VOGE), Goodenough Bay (GOOD), and D'Entrecasteaux Islands (DEI) blocks are treated as one unified block rotating about one pole. *F* tests cannot statistically distinguish between models where VOGE and GOOD are considered individual blocks (configuration 1) and ones where they are one unified block (configuration 2). Therefore, we treat them as one block in all TDEFNODE block models.

CSIRO ID	Field Sample #	Fault rock	Lat. (°S), Long (°E) (WGS84)	Quantitative mineralogy
42351	PNG14-19E	upper gouge	-9.82862, 149.44082	Corrensite/Saponite (65%), Augite (13%), Kaolin (8%), Amphibole (6%), Plagioclase (4%), Quartz (2%), Calcite (2%)
42352	PNG14-19F	lower gouge	-9.82862, 149.44082	Corrensite/Saponite (49%), Amphibole (18%), Augite (17%), Plagioclase (8%), Kaolin (4%), Quartz (1%), Calcite (3%)
42358	PNG14-33B	upper mafic gouge	-9.67726, 149.35904	Corrensite/Saponite (21%), Calcite (21%), Montmorillonite (11%), Plagioclase (11%), Epidote (9%), Kfeldspar (7%), Amphibole (5%), Quartz (5%), Chlorite (4%), Dolomite/Ankerite (3%), White mica (3%)
42357	PNG14-33A	lower mafic gouge	-9.67726, 149.35904	Plagioclase (30%), Epidote (18%), Amphibole (16%), Corrensite/Saponite (8%), Chlorite (7%), Titanite (6%), Stilpnomelane (6%), Quartz (3%), Calcite (3%), Kfeldspar (2%)
52980	PNG16-17-D2H	foliated cataclasite	-9.8297, 149.4403	Epidote (26%), Plagioclase (19%), Quartz (20%), Calcite (12%), Amphibole (9%), Corrensite/Saponite (8%), Chlorite (3%), Titanite (3%)
52979	PNG16-151E	foliated cataclasite	-9.6790, 149.2941	Amphibole (37%), Plagioclase (29%), Epidote (22%), Chlorite (5%), Titanite (3%), Calcite (2%), White mica (2%), Quartz (<1%)
45071	PNG15-70	serpentinite	-9.82863, 149.61246	Lizardite Serpentine (82%), Magnesite (12%), Saponite (4%), Maghemite (1%), Quartz (<1%), Calcite (<1%), Dolomite/Ankerite (<1%)
45070	PNG15-50B	ultracataclasite	-9.67778, 149.28669	Corrensite (25%), Kfeldspar (22%), Plagioclase (20%), Amphibole (16%), Augite (12%), Chlorite (2%), Calcite (2%), Quartz (1%)

Table S6. Description and quantitative mineralogy of fault rock samples.

Exp.	*Sample #*	σ_n^{eff} *(MPa)*	P_f *(MPa)*	*T (ºC)*	μ_{ss}
u368*	PNG-14-19F	30-60-90-120	20-40-60-80	50-100-150-200	0.24-0.18-0.19-0.26
u369*	PNG-14-19E	30-60-90-120	20-40-60-80	50-100-150-200	0.14-0.11-0.13-0.13
u370	PNG-14-19F	30-60-90-120	20-40-60-80	50-100-150-200	0.23-0.21-0.20-0.28
u371	PNG-14-19E	30-60-90-120	20-40-60-80	50-100-150-200	0.15-0.13-0.11-0.14
u487	PNG-15-50B$^{\wedge}$	120-150	80-100	200-250	0.63-0.74
u493	PNG-15-50B	90-120-150-180	90-120-150-180	150-200-250-300	0.59-0.59-0.66-0.72
u495	PNG-15-70	90-120-150-180	90-120-150-180	150-200-250-300	0.37-0.41-0.48-0.57
u496	PNG-15-70	120-150-180-210	80-100-120-140	300-350-400-450	0.50-0.60-0.62-0.63
u497	PNG-15-50B	120-150-180-210	80-100-120-140	300-350-400-450	0.75$^{\#}$-0.80-0.80-0.73
u545	PNG-14-33B	30-60-90-120	20-40-60-80	50-100-150-200	0.22-0.26-0.28-0.35
u546	PNG-14-33A	30-60-90-120	20-40-60-80	50-100-150-200	0.41-0.46-0.50-0.56
u547	PNG-14-33A	30-60-90-120	20-40-60-80	50-100-150-200	0.40-0.44-0.48-0.57
u772	PNG-16-17D2H	90-120-150-180	60-80-100-120	150-200-250-300	0.75-0.72-0.73-0.72$^{\#}$
u773	PNG-16-151e	90-120-150-180	60-80-100-120	150-200-250-300	0.66-0.60-0.59-0.57
u774	PNG-16-17D2H	120-150-180-210	80-100-120-140	300-350-400-450	0.57-0.60-0.47-0.44
u775	PNG-16-151e	120-150-180-210	80-100-120-140	300-350-400-450	0.67-0.67-0.66$^{\#}$-0.61

Table S7. List of experiments performed with experimental conditions and values of friction (=shear stress / effective normal stress, ignoring cohesion) at the end of each run-in (at 1 mm/s). The sliding velocity was 1 mm/s initially and then stepped to 0.3-1-3-10-30 mm/s with 0.5-1.5-1.5-1.5-1.5 mm of displacement. Steady state friction (m_{ss}) is determined at the end of the run-in at 1 mm/s at each s_n^{eff}-T-P_f condition. * Run-in at 10 mm/s, step from 0.3 to 1 mm/s omitted, step from 30-100 mm/s included, ^ experiment terminated prematurely due to pore fluid leak, $^{\#}$ indicates peak value of stick-slip.